

https://dspace.org/

The development of a burn-in test station at Wits for the Phase-II upgrade of the Tile Calorimeter of the ATLAS experiment

Njara, Nkosiphendule

2023-07

University of the Witwatersrand, Johannesburg

https://hdl.handle.net/10539/42346

Njara, Nkosiphendule. (2023). The development of a burn-in test station at Wits for the Phase-II upgrade of the Tile Calorimeter of the ATLAS experiment. [Master's dissertation, University of the Witwatersrand, Johannesburg]. https://hdl.handle.net/10539/42346

Downloaded from a DSpace repository. https://dspace.org/

The development of a burn-in test station at Wits for the Phase-II upgrade of the Tile Calorimeter of the ATLAS experiment.

Nkosiphendule Njara

Supervisor:

Professor Bruce Mellado



In partial fulfillment of the requirements for the degree of Master of Science

in the

School of Physics and Institute for Collider Particle Physics

University of the Witwatersrand, Johannesburg

10 July 2023

Declaration

I, Nkosiphendule Njara, declare that this report is my own, unaided work. It is being submitted in partial fulfillment of the requirements for the degree of Master of Science at the University of the Witwatersrand, Johannesburg. I affirm that this work has not been submitted for any degree or examination at any other university.



Nkosiphendule Njara

10 July 2023

Abstract

The University of the Witwatersrand is responsible for producing over 1200 Low Voltage Power Supply (LVPS) bricks to power the on-detector electronics of the Tile Calorimeter (TileCal) of the ATLAS detector in preparation for the Phase II upgrade. The LVPS brick is a DC/DC switch-mode power supply module that steps down a 200 VDC input to a 10 VDC output. Before being sent to CERN for installation, the LVPS bricks must undergo a quality assurance test. To ensure that these electronic devices meet the necessary standards for high-quality and reliability, the University of the Witwatersrand employs a burn-in test station that subjects them to electronic tests at elevated temperatures and other stressful conditions. The burn-in test station comprises of different Printed Circuit Boards (PCBs), each responsible for various functions, and a PIC microcontroller needs to be programmed for each board to perform its respective functions. An assembler MPLABX IDE and a compiler (CCS) are used for programming the PIC microcontroller, and the Labview software is used as the control program for the burn-in test station. A simulation was used in Proteus software to test the firmware functionality before programming the hardware. Preliminary results of the current version (version 8.4.2) of the LVPS brick are discussed.

Acknowledgements

I would like to express my sincere gratitude to my supervisor Prof Bruce Mellado for his invaluable guidance and support throughout this project. Their expertise in the field of high-energy physics, particularly in the area of Tile Calorimeters, was instrumental in helping me understand the complex workings of the ATLAS detector. I would also like to thank the members of the TileCal group at CERN for their helpful discussions. Their collective knowledge and expertise in the design, operation, and calibration of the TileCal system provided me with a deep insight into the workings of the ATLAS detector. I would like to acknowledge the financial support provided by the NRF. Without this support, this research would not have been possible. I am grateful to my family and friends for their constant support and encouragement throughout my studies. Their unwavering belief in me has been a source of strength and inspiration. Finally, I would like to extend my gratitude to following members of the Institute for collider particle physics, Dr Edward Nkadimeng, Thabo Lepota, Roger Van Rensburg and Ryan Mckenzie.

Contents

Declaration i

Abstract ii

Acknowledgements iii

List of Figures vii

List of Tables x

List of Abbreviations xi

1 The Large Hadron Collider (LHC) 1

1.1 Introduction 1

1.2 LHC experiments 4

1.2.1 Compact Muon Solenoid (CMS) 6

1.2.2 A Large Ion Collider Experiment (ALICE) 7

1.2.3 LHCb 8

1.3 HL-LHC upgrade 9

2 The ATLAS detector 12

2.1 Overview 12

2.2 ATLAS Inner Detector 14

2.2.1 The Muon Spectrometer . . . 17
2.2.2 Trigger and Data Acquisition system (TDAQ) . . . 18
2.2.3 Magnet system . . . 19
2.2.4 The ATLAS Phase II upgrade . . . 21

3 Tile Calorimeter 23
3.1 Phase II upgrade architecture . . . 27
3.1.1 Mechanics . . . 27
3.1.2 Main board (MB) . . . 27
3.1.3 Daughter Board (DB) . . . 28
3.1.4 Auxiliary (AUX) board . . . 29
3.1.5 The Front-End board . . . 30
3.1.6 Photomultiplier blocks . . . 31
3.1.7 High Voltage Power Supply . . . 31

4 LVPS system 32
4.1 Introduction . . . 32
4.2 DC/DC Switching Power Supply Module - LVPS Brick . . . 33
4.2.1 Low voltage power distribution . . . 37
4.2.2 200VDC Bulk Power Supplies . . . 37

5 Burn-in test station 39
5.1 Introduction . . . 39
5.2 Burn-in test station electronic hardware . . . 40
5.2.1 Printed Circuit Boards (PCBs) . . . 40
5.2.2 Mainboard . . . 41
5.2.3 Brick Interface . . . 42

5.2.4 Load Interface 43
5.2.5 Dummy load 44
5.3 Software 46
5.3.1 Embedded firmware 46
5.4 PIC16F883 microcontroller 46
5.4.1 Load-interface board circuitry simulation in Proteus 8 . . 48
LabView control program 50
5.5 Method(s) 51
5.5.1 Programming the PIC16883 microcontroller 51
5.5.2 Burn-in test station Procedure for the LVPS brick testing. 52
5.6 Results 53
5.6.1 Temperature monitoring using Themography 53
5.6.2 Monitoring the LVPS brick and high voltage power supply voltages and currents. 56

6 Conclusion **62**
6.1 LVPS brick production 62
6.2 Burn-in test station hardware and software 63
6.3 Results 64

Bibliography **66**

List of Figures

1.1 The CERN accelerator complex. The Schematic diagram shows the LHC collider with SPS as an injector and four interaction regions (ATLAS, CMS, ALICE and LHCb) [5]. 4
1.2 Inside view of the LHC tunnel [6] 5
1.3 The current schedule for the LHC and HL-LHC upgrade and run. Presently, the beginning of the HL-LHC run is predicted for mid-2026 [9] 10

2.1 A view of the ATLAS detector from the side. The detector has a height of 25 meters and a length of 44 meters [10]. 14
2.2 The Inner detector of the ATLAS experiment, showing the main components of the Inner Detector, SCT, Pixel detector, and TRT [15]. 16
2.3 (a) The ATLAS ID longitudinal view and (b) transverse view [16]. 17
2.4 ATLAS Phase II upgrade. 20

3.1 The ATLAS Tile and Liquid Argon Calorimeters are depicted in this schematic diagram [23]. 23

3.2 The TileCal cell layout, identified by a letter (A to E) followed by an integer number. The A-layer is the one that is closest to the beam line. On each side of $\eta = 0$, the naming convention is repeated [28]. 25
3.3 Tile Calorimeter wedge module. The various components of the optical readout, namely the tiles, the fibres and the photomultipliers, are shown [29]. 26
3.4 The phase II upgrade electronics [30]. 27

4.1 Schematic of the low voltage power distribution system. [32]. . . 33
4.2 Systematic diagram showing the location of the LVPS brick in the ATLAS detector 34
4.3 Systematic diagram of the LVPS brick [34]. 35
4.4 Wits Low Voltage power supply brick. The LVPS is custom-built using only COTS (Commercial Off-The-Shelf) components). (a) Shows the brick front view and (b) is the back view of the brick. 36

5.1 The reliability bathtub curve showing the three main periods, infant mortality, normal/"useful life" and end-of-life wear-out. . 41
5.2 Block Diagram of Burn-in Test Station showing Interconnections among PCBs (Mainboard, Brick Interface, Load Interface, and Dummy Load) and High Voltage Power Supply 42
5.3 The Burn-in test station Brick interface board. 43
5.4 Two Burn-in test station dummy load interface. 44

5.5 The PIC16F883 microcontroller (left) and the pin diagram of the microcontroller (right). 47
5.6 LTC2440 ADC. 49
5.7 In Proteus, a load interface circuit was created to simulate the PIC C microcontroller firmware. 50
5.8 Labview graphic user interface (Front panel). 51
5.9 The visible and infrared regions of the Electromagnetic spectrum zoomed out. 55
5.10 Thermogram showing one Low Voltage Power Supply "brick" operating in Burn-in test station. 56
5.11 Dummy load operating in burn-in station 57
5.12 Temperature 2 stability plot for the LVPS brick. 58
5.13 Temperature 2 stability plot for the LVPS brick. 58
5.14 Comparison of the brick input and output current against time. 60
5.15 Comparison of the LVPS brick input voltage with the set voltage by the high voltage power supply over time. 61
5.16 Comparing the brick set current and load current of the LVPS brick against time. 61
5.17 Comparison of the LVPS brick output and output load against time. 61

List of Tables

1.1 Perfomance parameters. 3

2.1 The parameters of each subsystem of the Inner Detector 16

5.1 Burn-in test station operating conditions. 53

5.2 A list of LVPS brick test parameters limit responses for output measurements [35]. 60

List of Abbreviations

LVPS - Low Voltage Power Supply

TileCal - Tile Calorimeter

LHC - Large Hadron Collider

HL-LHC - High-Luminosity Large Hadron Collider

ATLAS - A Toroidal LHC Apparatus

CERN - European Organisation for Nuclear Research

CMS - The Compact Muon Solenoid

ALICE - A Large Ion Collider Experiment

LHCb - The Large Hadron Collider beauty

IC -Integrated Circuits

PCB -Printed Circuit Board

pp - Proton-proton

T - Tesla

Fb^{-1} – Inverse Femtobarns

TeV – Tera electron volt

GeV – Giga electron volt

EU – European Union

USA – United States of America

EC – Electron Collider

FP7 – Frame work Program Seven

HiLumi – High Luminosity

W – Boson Wuon

Z - Boson Zeton

t - tonne

ID – Inner Detector

EM – Electromagnetic

High-pT – High transverse Momentum

B-physics - beauty physics

SCT -Semiconductor Tracker

R&D - Research and Development

TRT – Transition Radiation Tracker

HEC - Hadronic Endcap Calorimeter

FCal - Forward Calorimeter

MS - Muon Spectrometer

RPC - Resistive Plate Chambers

GJ - Giga Joules **TDAQ** – Trigger and Data Acquisition System

DAQ – Data Acquisition

CPU – Central Processing Unit

WLS – Wave Length Shifting

MBST – Minimum Bias Trigger Scintillators

LAr – Liquid Argon

MHz – Mega Hertz

ASCII – American Standard Code for Information Interchange

fLVPS – finger Low Voltage Power Supplies

AUX – Auxiliary Boards

V – Volts

LVBOXes – Low Voltage Boxes

A – Ampere

VDC – Volt Direct Current

VAC – Volt Alternating Current

DC – Direct Current

AC – Alternating Current

MB – Main Board

FENICS - Front End board for the New Infrastructure with Calibration and signal Shaping

DB – Daughter Board

PMT – Photomultiying tube

FPGA – Field-programmable Array

ADC – Analog to Digital Converter

sROD - super Read-Out Driver

Gbps – Giga bits per second

GBT – Giga Bits Transceiver

QSFP - Quad Small Form-Factor Pluggable

DCS - Detector Control Systems

AUX – Auxiliary

ELMB – Embedded Local Monitor Board

HV – High Voltage

CAN – Controller Area Network

PCB – Printed Circuit Board

UART - Universal Asynchronous Receiver-Transmitter

USB – Universal Serial Bus

RTS – Request To Send

PC – Personal Computer

COM Port - Communication Port

PIC – Peripheral Integrated Circuit

MOSFET - Metal–Oxide–Semiconductor Field-effect Transistor

IDE – Integrated Development Environment

CCS - Custom Computer Services

ASCII - American Standard Code For Information Interchange

LED - Light-Emitting Diode

LTC - Linear Technology

(LBA-LBC) - Long Barrel

(EBA-EBC) - External Barrel

FLIR - Forward Looking Infrared Radiometer

Chapter 1

The Large Hadron Collider (LHC)

1.1 Introduction

The Large Hadron Collider (LHC) is a 26.7-kilometer long hadron collider situated in Geneva, spanning the French-Swiss border. Built at the European Organization for Nuclear Research (CERN), the LHC aims to explore the energy frontier of particle physics [1]. Approved in 1994, it became operational for data collection in 2009, following the successful completion of its design and construction, which involved overcoming numerous technical and logistical challenges. The LHC has since undergone three operational periods: Run 1, Run 2, and the ongoing Run 3, each lasting approximately four years. These runs have generated an impressive amount of data, with an approximate integrated luminosity of 196 fb^{-1} for Runs 1 and 2, and a projected total of 500 fb^{-1} for Run 3. As the stored beam energy increased, the operation of the machine presented various challenges, which will be further explored. Being the largest and most powerful particle accelerator worldwide, the LHC consists of superconducting magnets that facilitate proton collisions at a center-of-mass energy of $\sqrt{s} = 14$ TeV, resulting in an instantaneous luminosity of $\ell =$

2×10^{34} $cm^{-2}s^{-1}$. Additionally, the LHC can collide heavy (Pb) ions with a peak luminosity of 10^{27} $cm^{-2}s^{-1}$ and a nucleon energy of 2.8 TeV [1]. With collision energies reaching up to 14 TeV, the LHC aims to probe physics beyond the Standard Model. It successfully commenced proton-proton collisions in 2010 at a center-of-mass energy of 7 TeV, followed by operating at 8 TeV from April 2012 until the end of 2013 [2]. Notably, on July 4, 2012, CERN made a groundbreaking announcement, confirming the existence of a modern Higgs boson with a mass of approximately 125 GeV. This discovery represents a significant milestone in the search for the elusive Higgs particle, with the potential to unlock further groundbreaking insights. The LHC's core function revolves around colliding opposing beams of protons. This proton-proton (pp) collisions occur when the beams reach an energy level of 7 TeV each [3]. The beams traverse the LHC ring within a vacuum, guided by superconducting magnets maintained at low temperatures through a cryogenic system. The superconducting cables facilitate current flow without resistance when in their superconducting state. Throughout hours of operation, the beams maintain high energy levels while collisions take place within the four primary LHC experiments. Comprised of bunches containing billions of protons, the beams travel at speeds slightly below that of light. They are injected, accelerated, and continually circulated for hours, guided by thousands of powerful superconducting magnets. While most sections of the ring feature separate vacuum pipes for each beam, the beams collide at four specific points housing the primary experiments, known as ALICE, ATLAS, CMS, and LHCb [4].

TABLE 1.1: Perfomance parameters.

Circumference	26.7 km
Beam energy at collision	7 TeV
Beam energy at injection	0.45 TeV
Dipole field at 7 TeV	8.33 T
Luminosity	10^{34} cm^{-2}s^{-1}
Beam current	0.56 A
Protons per bunch	1.1×10^{11}
Number of bunches	2808
Nominal bunch spacing	24.95 ns
Normalized emittance	3.75µm
Total crossing angle	300µrad
Energy loss per turn	6.7 keV
Critical synchrotron energy	44.1 eV
Radiated power per beam	3.8 kW
Stored energy per beam	350 MJ
Stored energy in magnets	11 GJ
Operating temperature	1.9K

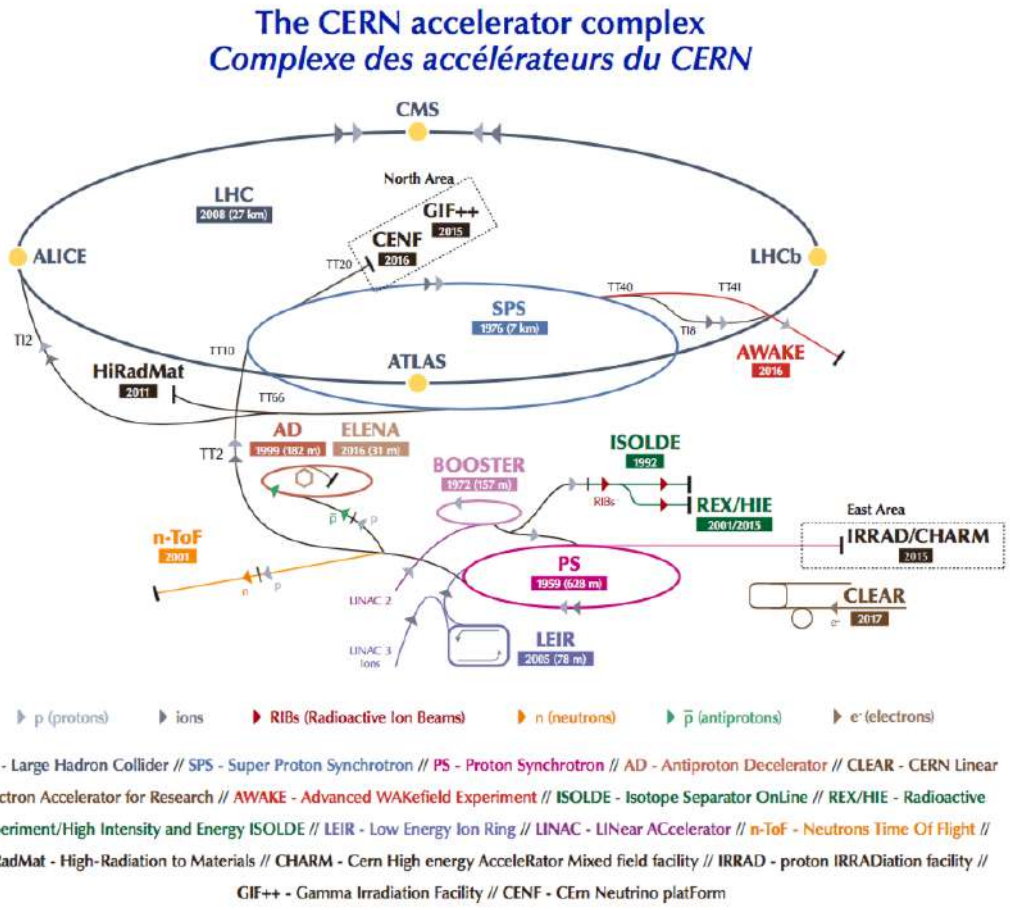


FIGURE 1.1: The CERN accelerator complex. The Schematic diagram shows the LHC collider with SPS as an injector and four interaction regions (ATLAS, CMS, ALICE and LHCb) [5].

1.2 LHC experiments

The Large Hadron Collider (LHC) hosts a comprehensive array of eight experiments dedicated to exploring the multitude of particles generated through collisions within the accelerator. These experiments are carried out through international collaborations of scientists from various institutes. Every experiment possesses its own distinct character, shaped by the specific detectors it employs. The two largest experiments, ATLAS and CMS, use general-purpose



FIGURE 1.2: Inside view of the LHC tunnel [6]

detectors to explore a wide range of physics. Constructing independent detectors is crucial to confirm any new discoveries. In contrast, the detectors in ALICE and LHCb are designed to focus on specific phenomena. All four detectors are located underground in vast caverns along the LHC ring. Subsequent subsections discuss the three experiments CMS, ALICE, and LHCb, while Chapter 2 provides more detailed information on ATLAS.

TOTEM and LHCf focus on "forward particles" – protons or heavy ions that do not collide head-on. These are the smallest experiments on the LHC. LHCf is composed of two detectors located 140 meters on either side of the ATLAS collision point along the LHC beamline. TOTEM uses detectors on either side of the CMS interaction point. MoEDAL-MAPP is searching for a hypothetical particle called the magnetic monopole, using detectors placed near the LHCb. FASER, the newest LHC experiment, is located 480 meters away from the ATLAS collision point to search for light new particles and explore neutrinos.

1.2.1 Compact Muon Solenoid (CMS)

At the Large Hadron Collider, the Compact Muon Solenoid (CMS) is a general-purpose detector (LHC). Its physics research ranges from the Standard Model (which includes the Higgs boson) to the quest for extra dimensions and particles that could make up dark matter. It uses distinct technical solutions and a different magnet-system design than the ATLAS experiment but has the same scientific goals. The detector is used in CERN's Large Hadron Collider (LHC). It was designed to explore proton-proton (and lead-lead) collisions at 14 TeV (5.5 TeV nucleon-nucleon) and luminosities up to 10^{34} $cm^{-2}s^{-1}$ (10^{27} $cm^{-2}s^{-1}$) at a center-of-mass energy of 14 TeV (5.5 TeV nucleon-nucleon) [7]. A large-bore superconducting solenoid with a high magnetic field surrounds an all-silicon pixel and strip tracker, a lead-tungstate scintillating-crystals electromagnetic calorimeter, and a brass-scintillator sampling hadron calorimeter in the heart of the CMS detector. The flux-iron return's yoke is equipped with four stations of muon detectors that cover the majority of the 4 solid angles. Forward sampling calorimeters improve hermeticity by extending pseudorapidity coverage to high values ($|\eta| \leq 5$). The CMS detector has a total length of 21.6 m, a width of 14.6 m, and a weight of 12500 t [8].

The following is a summary of the detector requirements for CMS to satisfy the LHC physics program goals:

- The requirements include effective identification of muons, accurate momentum resolution across a broad range of momenta and angles, precise resolution of dimuon mass ($\approx 1\%$ at 100 GeV), and unambiguous determination of the muon charge for momentum less than <1 TeV.;

- The inner tracker should possess a high resolution and efficiency in reconstructing charged-particle momentum. Additionally, efficient triggering and offline tagging of τ's and b-jets should be achievable by having pixel detectors situated close to the interaction region.

- The requirements for the detector include excellent resolution in measuring electromagnetic energy, precise mass resolution for diphoton and dielectron events (approximately 1% at 100 GeV), broad coverage in space, effective rejection of π^0 particles, and efficient isolation of photons and leptons even under high luminosities;

- A fine lateral segmentation hadron calorimeter with large geometric coverage is required to achieve good resolution for missing transverse energy and dijet mass.

1.2.2 A Large Ion Collider Experiment (ALICE)

ALICE is a heavy-ion detector that focuses on QCD, the strong-interaction sector of the Standard Model, at the CERN LHC. It is intended to investigate the physics of strongly interacting matter and the quark-gluon plasma in nucleus-nucleus collisions at extreme values of energy density and temperature. The physics program encompasses lighter ion collisions, lower energy running, and dedicated proton-nucleus runs, in addition to the primary Pb ion program. ALICE will also collect reference data for the heavy-ion program and explore various QCD topics that complement other LHC detectors using proton beams at the top LHC energy. The ALICE detector, which weighs around 10,000 t and has a total volume of 161626 m^3, was developed by a team of over 1000

physicists and engineers from 105 institutions across 30 countries. The experiment consists of 18 separate detector systems, each with its own technology choices and design constraints dictated by the physics needs and projected experimental circumstances at the LHC. The most challenging design constraint is dealing with the high particle multiplicity expected at the center of Pb-Pb collisions. The various subsystems were optimized to provide high momentum resolution and excellent particle identification (PID) over a wide range of momenta, up to the maximum multiplicities expected at the LHC, enabling a detailed study of hadrons, electrons, muons, and photons created in heavy nucleus collisions.

1.2.3 LHCb

At the LHC, LHCb is an experiment dedicated to heavy flavour physics. Its main purpose is to hunt for indirect evidence of novel physics in CP violation and uncommon hadron decays. The LHCb experiment focuses on examining a type of particle known as the "beauty quark", to better understand the subtle differences between matter and antimatter. Rather than using an enclosed detector to encircle the entire collision location, as ATLAS and CMS do, the LHCb experiment uses a sequence of subdetectors to detect predominantly forward particles - those propelled forward in one direction by the collision. The first subdetector is placed at the collision point, with the others trailing behind it for a distance of 20 meters. The Large Hadron Collider (LHC) is responsible for producing six different types of quarks. Quarks are fundamental particles that make up all matter. Up, down, charm, strange, top, and bottom quarks are among the six flavors. These distinct quark flavors are created

through high-energy collisions assisted by the LHC and then interact with other particles. The ensuing decay processes that occur after their production allows for the study of quarks' fundamental properties and behaviors, leading to our understanding of matter's underlying structure. LHCb has constructed advanced movable tracking detectors close to the path of the circular beams in the LHC to collect the b quarks. A forward spectrometer and planar detectors make up the 5600 t LHCb detector. It's 21 meters long, 10 meters tall, and 13 meters broad, and it's located 100 meters below near Ferney-Voltaire, France.

1.3 HL-LHC upgrade

The High-Luminosity LHC, an extensive upgrade of the Large Hadron Collider (LHC), began as a design study supported by the European Union and partners from the EU, USA, and Japan. Its purpose is to enhance the LHC's performance, which is measured by luminosity - the amount of potential collisions per surface unit during a certain length of time. The High-Luminosity LHC aims to increase the number of collisions by a factor of between five and ten, allowing physicists to study the fundamental components of matter and the forces that bind them together in greater detail. This will produce more data, enabling the examination of known mechanisms and identifying new phenomena. The High-Luminosity LHC is expected to produce up to 4000 fb^{-1} of proton-proton collisions at 14 TeV center-of-mass energy, with an instantaneous luminosity projected to reach up to 7.5×10^{34} $cm^{-2}s^{-1}$, a four-fold increase beyond Run 2. The CMS experiment is gearing up for major detector upgrades to prepare for the HL-LHC, which aims to collect at least 3000 fb^{-1}

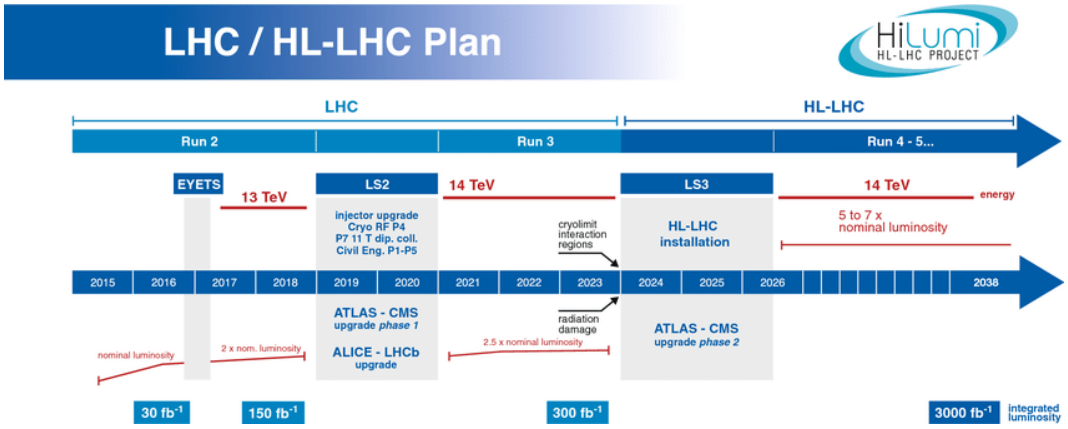


FIGURE 1.3: The current schedule for the LHC and HL-LHC upgrade and run. Presently, the beginning of the HL-LHC run is predicted for mid-2026 [9]

integrated luminosity over ten years of operations. It is estimated that the HL-LHC will produce about 15 million Higgs bosons annually, compared to three million by the LHC in 2017.

To increase the luminosity, the number of collisions must be increased. In the core of the ATLAS and CMS detector, no less than 140 collisions will be delivered each time the particle bunches meet, compared to around 40 currently. This requires a more intense and focused beam than the one used in the LHC. The HL-LHC project involves installing new equipment and removing the existing LHC equipment over a 1.2 km length of the 27 km LHC. New, more capable superconducting quadrupole magnets made of niobium-tin will be installed on both sides of the ATLAS and CMS experiments to better focus the beams. These magnets can achieve higher magnetic fields than the current LHC magnets made of niobium-titanium, 12 T compared to 8 T. Production of 24 quadrupole magnets is currently underway. This new superconducting equipment will give the particle bunches a transverse momentum before they

meet, increasing the overlap area of the two bunches and thus the probability of collisions. Additionally, 16 crab cavities will be installed on each side of the ATLAS and CMS experiments.

Chapter 2

The ATLAS detector

2.1 Overview

ATLAS uses a right-handed coordinate system, with the nominal interaction point (IP) as its origin. The z-axis is defined by the beam direction, with the positive x-axis pointing from the IP to the LHC ring's center and the positive y-axis pointing upwards. In the transverse plane, cylindrical coordinates (r,ϕ) are employed, and pseudorapidity is defined as $|\eta| = \ln \tan(\varphi/2)$ in terms of the polar angle.

A barrel area and two endcaps make up the ATLAS detector, with each region containing many detector subsystems. The Inner Detector (ID), which is closest to the contact site, performs charged particle tracking out to $|\eta|$ of 2.5. The Pixel Detector and the Semi-Conductor Tracker (SCT) and the Transition Radiation Tracker (TRT) are two silicon detectors immersed in a 2 T axial magnetic field provided by a superconducting solenoid magnet. Individual drift tubes with radiators form the basis of the TRT, which allows for electron identification. The ID is encircled by liquid argon electromagnetic (EM) calorimeters in the barrel and endcaps, which offer coverage out to $|\eta|$ of

3.1. The Hadronic Endcap Calorimeter (HEC) uses liquid argon and covers the range of $1.5 < |\eta| < 3.2$ in the endcap area. Additionally, a Forward Calorimeter (FCal) based on liquid argon is located in the same cryostat as the endcap EM calorimeter and the HEC, providing calorimetric coverage for the region $3.2 < |\eta| < 4.9$. The Muon Spectrometer (MS), located beyond the calorimeter system, utilizes a set of large superconducting air-core toroid magnets to generate a toroidal magnetic field in the barrel and endcap regions. The tracking coverage extends out to $|\eta|$ of 2.7 with planes of interleaved muon detectors, and the triggering extends out to $|\eta|$ of 2.4 in both regions. Figure 2.1 depicts the ATLAS detector. ATLAS is approximately 25 m tall and about 44 m long. It is around 7000 t in weight. ATLAS is a 100 m underground structure erected around the LHC beam pipe. One of the LHC collision locations is in the center of the detector. Particles created in collisions shoot out in all directions from the detector's center. ATLAS records the paths and energy of charged particles using the tracking systems and measures the energy of e/gamma and jets using the calorimeters.. The calorimeter system surrounds the ID. The liquid argon electromagnetic calorimeters, Tile calorimeters (discussed in detail in chapter 3), liquid argon hadronic end-cap calorimeters, and forward calorimeters make up the calorimeter system. Each of these is depicted in Figure 2.1. The calorimeters are used to determine how much energy electrons, photons, and hadrons have. They are sensitive to both charged and neutral particles. Lastly, the calorimeters are surrounded by the Muon Spectrometer (MS). The calorimeter system stops all particles except muons and neutrinos thus the MS is used to track muon trajectories. The MS is made up of muon chambers that operate in a magnetic field that is generated by toroid magnetics.

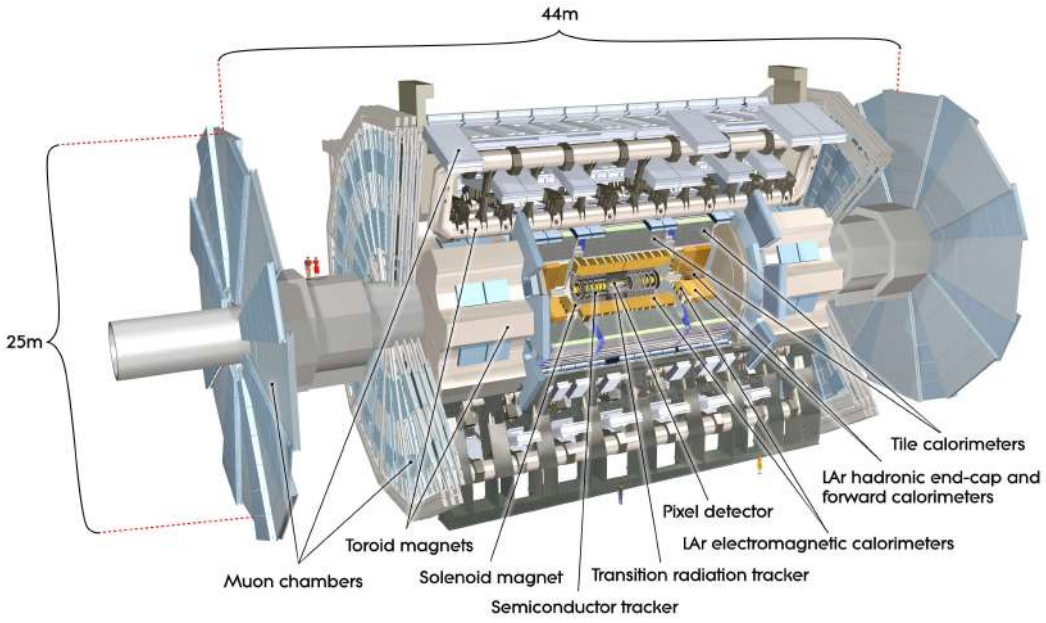


FIGURE 2.1: A view of the ATLAS detector from the side. The detector has a height of 25 meters and a length of 44 meters [10].

2.2 ATLAS Inner Detector

ATLAS Inner Detector (ID) tracks charged particles from the LHC beam-pipe to the electromagnetic (EM) calorimeter system. It distinguishes between signatures of electrons and photons, measures the charge sign of high-pT electrons, validates high-pT muons (the muon system measures their energy), provides lifetime b-jet and tau decay tagging, enables B-physics research by measuring lifetime as well as reconstructing exclusive states [11]. It is also involved in the Level-2 Trigger. The subsystems of the Inner Detector are Pixel Detector, Semiconductor Tracker (SCT), and Transition Radiation Tracker (TRT) [12]. The tracking detectors are the innermost layers of the ATLAS experiment. The beam pipe is surrounded by the tracking detectors, which cover the range of -2.5 $< \eta <$ 2.5, with full coverage in φ [13]. The parameters of each

system of the Inner Detector are shown in table 2.1. The ATLAS ID longitudinal view and transverse view is shown in figure 2.3a and 2.3b respectively. The pixel detector is meant to produce a collection of measurements with high granularity and precision as close to the interaction point as possible. The system determines the impact parameter resolution and the capacity of the Inner Detector to detect short-lived particles such as b-quarks and τ-leptons over the complete acceptance and gives three precision measurements. The SCT system is designed to deliver four precision measurements per track in the intermediate radial range, allowing for the measurement of momentum, impact parameter, and vertex location, as well as good pattern identification thanks to the high granularity [14]. The system has a surface area an order of magnitude larger than earlier generations of silicon microstrip detectors, and it must also deal with radiation levels that would change the fundamental features of the silicon wafers. The TRT is based on the employment of straw detectors, which, due to their small diameter and isolation of the sensing wires within separate gas envelopes, can operate at the extremely high rates required. The use of xenon gas to detect transition-radiation photons generated in a radiator between the straws adds electron identification capability. This technology is innately radiation resistant and enables for a large number of measurements on each track, typically 36, at a cheap cost. At the LHC design luminosity (10^{34} cm^{-2} s^{-1}), however, the detector must deal with massive occupancy and high counting rates.

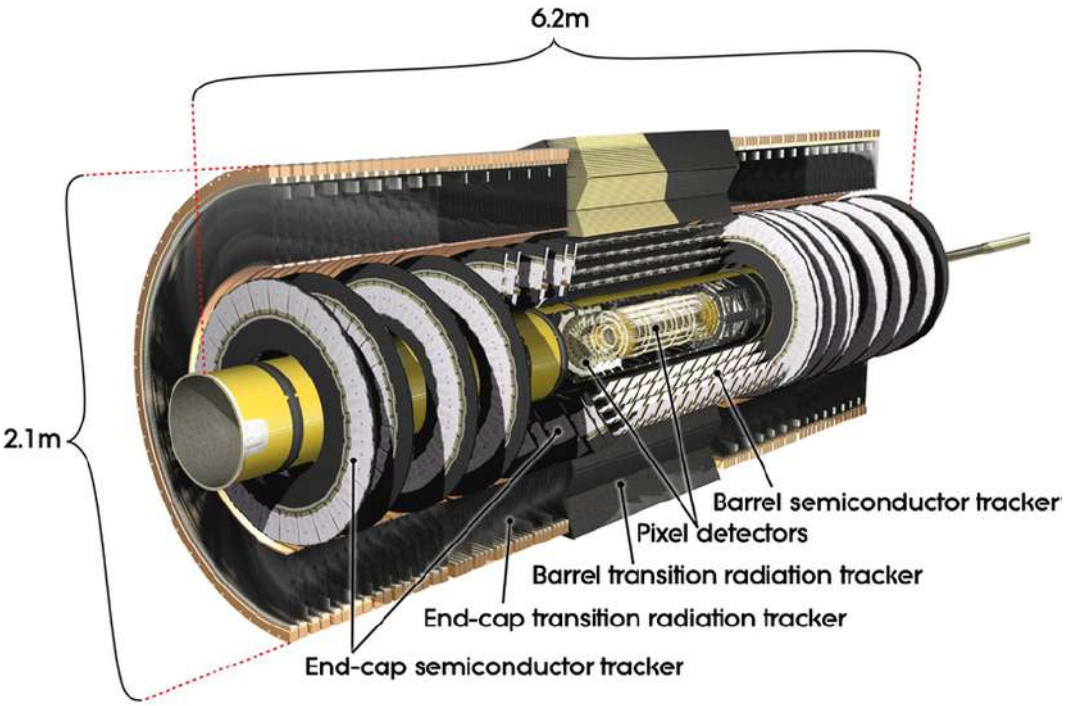
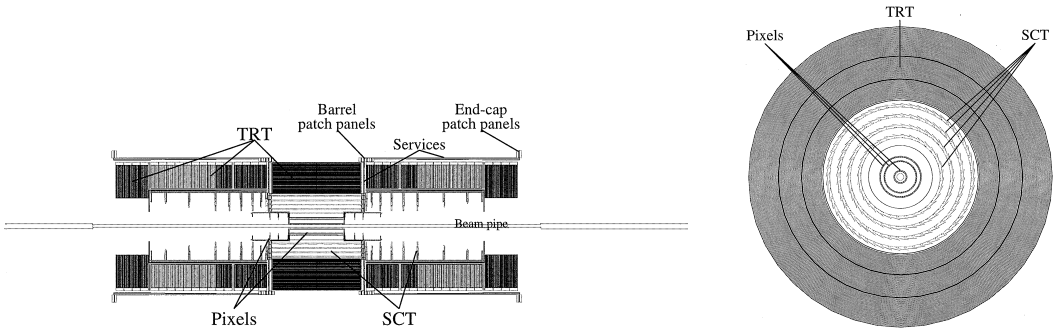


FIGURE 2.2: The Inner detector of the ATLAS experiment, showing the main components of the Inner Detector, SCT, Pixel detector, and TRT [15].

TABLE 2.1: The parameters of each subsystem of the Inner Detector

System	Position	Area (m^2)	Resolution σ (μm)	Channels (10^6)	η coverage
Pixels	1 removable barrel layer	0.2	Rφ = 12, z = 66	16	±2.5
	2 barrel layers	1.4	Rφ = 12, z = 66	81	±1.7
	4 end-cap disks on each side	0.7	Rφ = 12, R = 77	43	1.7-2.5
Silicon strips	4 barrel layers	34.4	Rφ = 16, z = 580	3.2	±1.4
	9 end-cap wheels on each side	26.7	Rφ = 16, R = 580	3.0	1.4–2.5
TRT	Axial barrel straws		170 (per straw)	0.1	±0.7
	Radial end-cap straws 36 straws per track		170 (per straw)	0.32	0.7–2.5



(A) Inner detector side view.

(B) Transverse view of the ATLAS Inner Detector.

FIGURE 2.3: (a) The ATLAS ID longitudinal view and (b) transverse view [16].

2.2.1 The Muon Spectrometer

Muons are particles that are very similar to electrons but they are 200 times more massive. They result from the decay of particles created by protons colliding in the ATLAS detector's core. The signals of the muons provide evidence about which particles emerged from the protons' collision. The detection of muons is performed by muon spectrometer. The ATLAS muon spectrometer is designed for excellent resolution at large transverse momentum [17]. Three massive superconducting air-core toroids, precision tracking chambers for accurate momentum resolution, and an effective trigger system based on chambers with a fast response make up the muon spectrometer. The physics program of ATLAS has placed a strong emphasis on durability and standalone high performance throughout a wide range of transverse momentum.

The Muon Spectrometer is divided into three regions: a Barrel covering $|\eta| \leq 1.2$ and two End-Caps covering the rapidity regions ($1 < |\eta| \leq 2.7$). The Barrel features eight massive superconducting coils arranged in an open geometry, creating a toroidal field whose integral varies from 2 to 5 Tm in the

Barrel, with considerable variation as a function of azimuth angle. The muon momentum is determined by calculating the sagitta of the muon trajectory induced by the magnetic field. Three high-precision measuring stations equipped with Monitored Drift Tubes are positioned inside the toroid, arranged in three cylindrical layers around the beam axis, to sample the muon spectrum. Each station can measure muon locations with a precision of approximately 50 meters, and provides angular information on the observed track segments, which aids in improving pattern recognition for the entire muon track reconstruction. The Barrel spectrometer also includes specialized trigger detectors called Resistive Plate Chambers (RPCs), with two layers of two RPC detectors in the center station generating a low pt trigger (pt $>$ 6 GeV/c), while the high pt trigger (pt $>$ 20 GeV/c) and low pt station are formed in the outer station using only one layer with two RPC detectors. The RPCs measure both the bending and non-bending coordinates, and the trigger is created by requiring quick (25 ns) coincidences in both the bending and non-bending planes that point to the interaction zone.

2.2.2 Trigger and Data Acquisition system (TDAQ)

The TDAQ is an online system that picks particle interactions of possible interest for physics analysis (trigger) and collects the relevant data from the detectors, converts it to a usable format, and stores it permanently (DAQ). Special modes of operation, such as the necessity to calibrate many detectors in parallel outside of typical data-taking intervals, must be considered. TDAQ is frequently interpreted to cover related functions like as run control, monitoring, clock distribution, and bookkeeping, which are all necessary for effective data

collecting and subsequent offline analysis. The ATLAS trigger system carries out the selection process in two stages. A subset of data from the calorimeters and the Muon Spectrometer is used by the first-level hardware trigger, which is built with custom-made electronics on the detector. The choice to maintain event data is decided fewer than 2.5 microseconds after the event has occurred. The event data is stored in storage buffers during this time. If the event is chosen, it is forwarded to the second-level trigger, which can handle up to 100,000 events per second. A massive farm of around 40,000 CPU cores powers the second-level software trigger. It conducts very extensive assessments of each collision event in just 200 microseconds, evaluating data from specific detector locations. Finally, the second-level trigger chooses roughly 1000 events per second for offline processing and sends them to a data storage system.

2.2.3 Magnet system

To measure the momentum of electrically charged particles, a strong magnetic field must be present throughout the detector. As the particles move through the magnetic field, they are affected by the Lorentz force, which is perpendicular to the particle velocity and the field's direction, B. This causes the particles to follow curved paths, with the radius of curvature proportional to momentum and the direction of curvature defined by the charge's sign. The solenoid magnet surrounding the Inner Detector and the toroid magnet system incorporated in the Muon Spectrometer are two types of superconducting magnet systems used in the ATLAS detector to provide the bending power required for the momentum measurement of charged particles. This magnetic system has a diameter of 20 meters and a length of 26 meters, with a stored

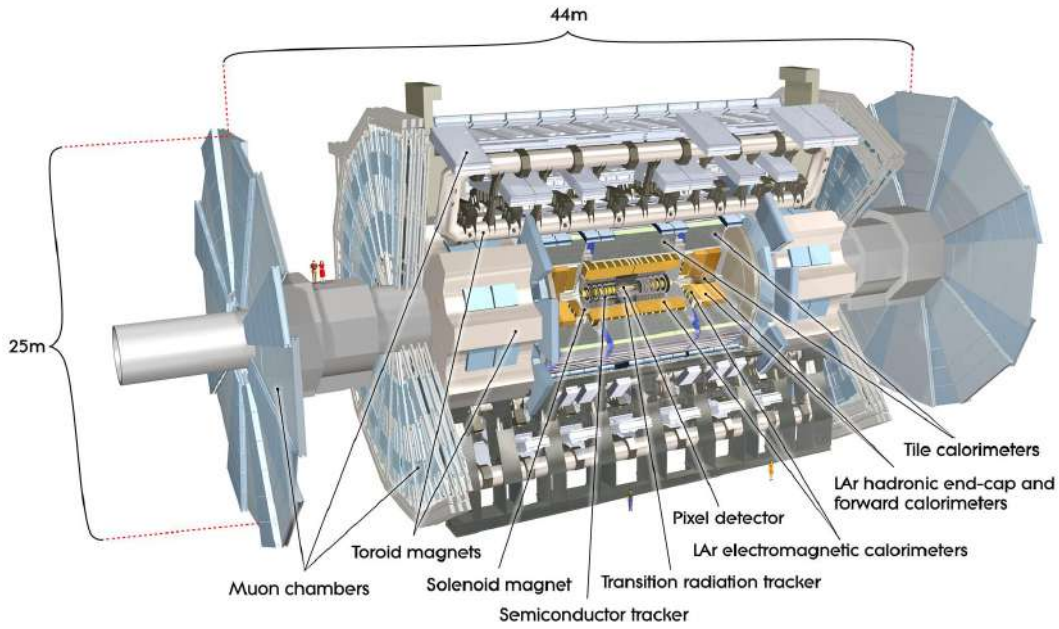


FIGURE 2.4: ATLAS Phase II upgrade.

energy of 1.5 GJ [18]. The central superconducting solenoid is positioned on the beam axis and is optimized to generate a 2 T axial magnetic field for the Inner Detector's momentum measurements while minimizing the radiative thickness in front of the barrel EM calorimeter [19]. The Muon Spectrometer's toroid magnet system generates a magnetic field for momentum measurement, with typical field strengths of 0.5 T and 1 T in the center and end-cap areas, respectively. Eight superconducting coils in the barrel and two toroids with eight coils each in the end-cap regions form a toroidal magnetic field that is perpendicular to the one of the solenoid [20].

2.2.4 The ATLAS Phase II upgrade

The Phase-II upgrade program is currently in its final stage of design and R&D. The construction and installation of the Phase-II upgrades has been delayed to 2027-2031. The ATLAS Phase-II program includes improvements to the detector's pixel and strip trackers, LAr and Tile calorimeters, muon system, trigger and data acquisition system. In the high-luminosity phase (HL), the Large Hadron Collider (LHC) at CERN will produce an integrated luminosity of up to 4000 fb^{-1} thanks to an increased instantaneous luminosity of up to 7.5×10^{34} cm^{-2} s^{-1} [21]. During Long Shutdown, the ATLAS detector will be upgraded. This modification will allow the detector to cope with the high luminosity, which will result in a 200-collision event pileup for each bunch-crossing. At LHC energies, the cross-section for inelastic, non-diffractive pp interactions is at the level of 70 mb [22]. The mean number of minimum bias events that should be observed by the Inner Detector at a design luminosity of 10^{34} cm^{-2} s^{-1} and a bunch spacing of 25 ns is 18. However, because about 20% of the LHC's bunches will be empty, the average time between them will be longer. The average number of collisions for these non-empty bunches has climbed to around 23. This means that when the trigger selects an intriguing event, there will be an average of 23 single minimum bias events superimposed, these are referred to as pile-up events. During the phase II upgrade, most readout electronics will be replaced. This will include the installation of the new LVPS in the radiation zone for on-detector electronics. The Low Voltage power supply is discussed in more detail in Chapter 4. During the HL-LHC operation, the on-detector front-end electronics for the LAr and Tile calorimeters will be subjected to substantially greater radiation levels. Many

of the ASICs used in the existing front-end electronics were not built to withstand the radiation environment of the HL-LHC. The proposed modifications to the front-end electronics will make use of technology advancements to provide a stable architecture that can operate in the HL-LHC environment. The modified electronics will also be capable of handling high digitization rates, large data quantities, and transmission speeds up to 140 TB/s at high luminosity. The new front-end board will enable analog to digital conversion at 40 MHz and will have a 16-bit dynamic range and allow multiplexing and serialization of data, as well as transmission across high-speed optical networks, are possible.

Chapter 3

Tile Calorimeter

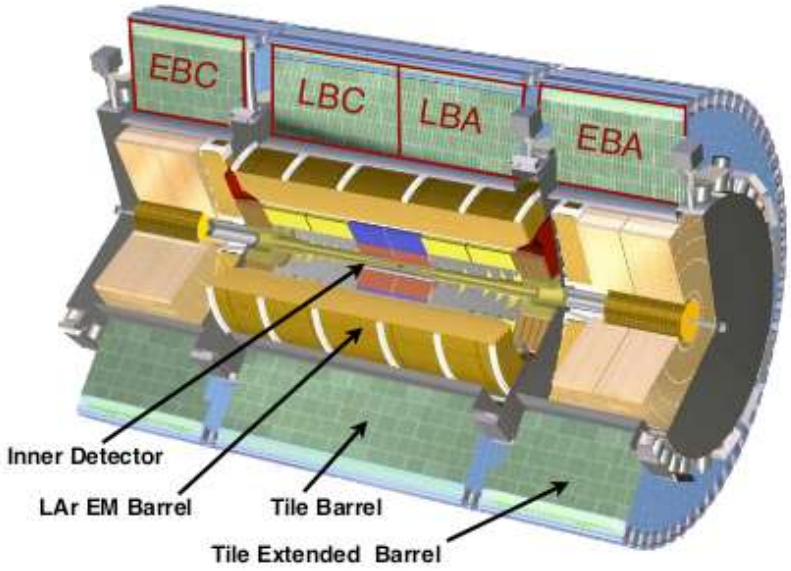


FIGURE 3.1: The ATLAS Tile and Liquid Argon Calorimeters are depicted in this schematic diagram [23].

The Tile Calorimeter (TileCal) is the ATLAS central Hadronic Calorimeter.. It uses plastic scintillating tiles as the active component and iron plates as the absorber. Wavelength-shifting fibers transmit the scintillation light generated in the tiles to photomultiplier tubes (PMTs). Before being sent to off-detector data-acquisition systems, approximately 10000 PMTs' electronic

output signals are monitored and digitized every 25 ns. The TileCal catches around 30% of jet energy and is used to measure jet and missing energy, as well as jet substructure, electron isolation, and triggering (including muon information) [24]. The central cylinder is called the Long Barrel (LB), and the two shorter cylinders surrounding it are called Extended Barrels (EB) in order to differentiate them from the Liquid Argon calorimeter endcaps with smaller radius. With an inner radius of 2.28 m and an outer radius of 4.23 m, the center long barrels (LBA, LBC) and end-cap barrels (EBA, EBC) form four logical sub-detectors. The two LB parts are 2.82 meters long each, and the EB sections are 2.91 meters long, for pseudo-rapidity up to 1.6. As shown in Figure 3.1, TileCal is a calorimeter with steel and plastic scintillator plates for sampling. Wavelength-shifting (WLS) fibres read out approximately 460,000 scintillators on each of the two sides [25]. Photomultiplier tubes (PMT) read out the WLS fibres, which are bundled to form cells. TileCal comprises 4672 readout cells, each equipped with two PMTs that receive light from opposite sides of every tile [26]. At $\eta = 0$, the barrels are split radially into three layers ("A", "BC", and "D"), with interaction lengths of 1.4, 3.9, and 1.8, respectively. With each A-B/C-D grouping creating a tower currently employed for the quick trigger, the $\eta \times \varphi$ granularity is roughly 0.1×0.1 [27]. In the region between the LB and the EB, the Tile system additionally reads out a system of scintillators (designated as E cells). The E1 and E2 "gap scintillators", as well as the E3 and E4 "cryostat" or "crack" scintillators, are used to quantify the energy exiting the electromagnetic calorimeter. The Minimum Bias Trigger Scintillators (MBTS) are used to monitor minimum-bias event rates at even higher η values, beneath the E4 scintillators.

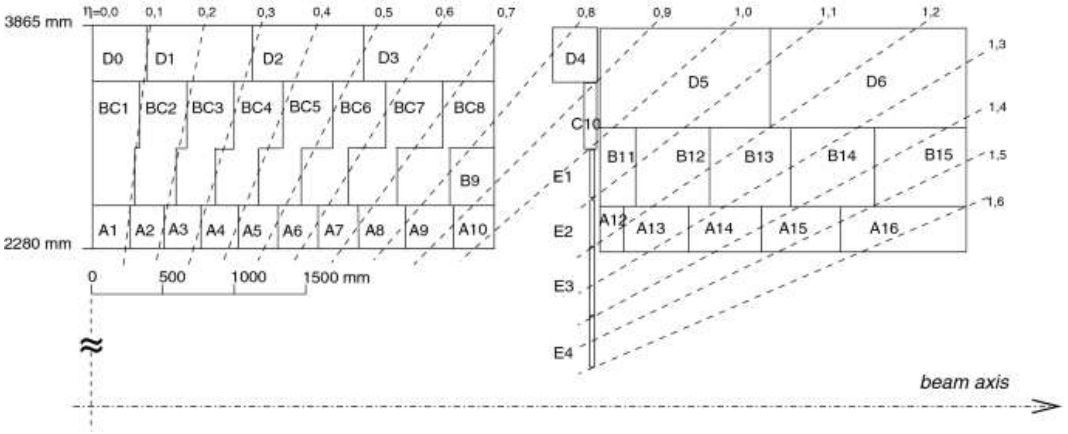


FIGURE 3.2: The TileCal cell layout, identified by a letter (A to E) followed by an integer number. The A-layer is the one that is closest to the beam line. On each side of $\eta = 0$, the naming convention is repeated [28].

The Tile barrels are segmented into 64 modules based on azimuth, with the module's outer radius containing electronics housed in a water-cooled "drawer". To power the drawers, "finger" low-voltage power supplies (LVPS) are positioned at the outer end of each drawer. The calorimeter steel shields the majority of the electronics from radiation. The LVPS, which have already proven vulnerability to neutron-induced latch-up during Run 1, are the most vulnerable to radiation.

The front-end electronics system serves multiple essential functions in the detector setup. It plays a key role in generating a rapid analog trigger signal by combining Photomultiplier Tube (PMT) signals from various cells, facilitating efficient event identification. Furthermore, the system digitizes PMT signals and combines continuous PMT current to analyze low-light processes, including gamma rays from the radioactive source calibration system and minimal bias events. The front-end electronics then serializes the data and transmits it to the back-end system for further processing. A dynamic range of 16 bits

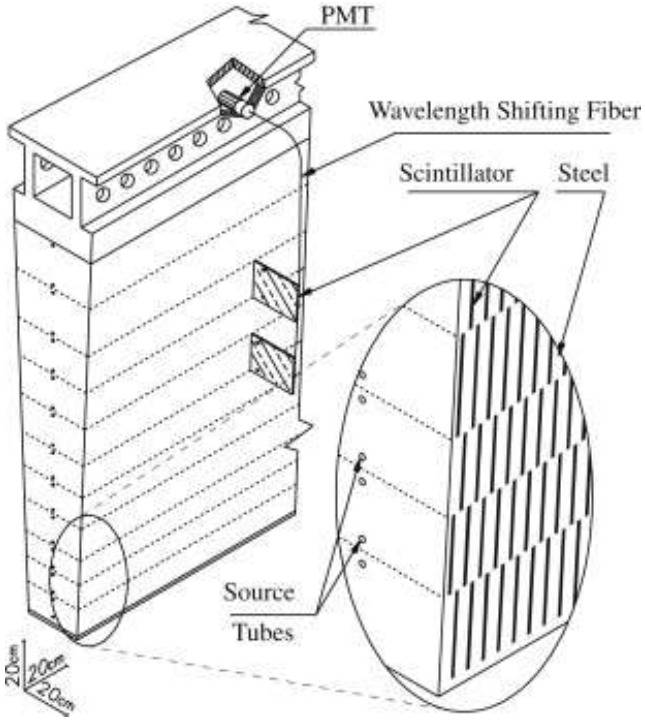


FIGURE 3.3: Tile Calorimeter wedge module. The various components of the optical readout, namely the tiles, the fibres and the photomultipliers, are shown [29].

is necessary to accommodate the readout requirements. Specifically, the Tile calorimeter is designed to detect single muons with energies of approximately 400 MeV in its smallest central cells while maintaining a linear response to measure jets with energies in the multi-TeV range.

Figure 3.3 show the tile calorimeter wedge module. The TileCal is made up of steel as absorber and plastic scintillating tiles as shown in the schematic diagram.

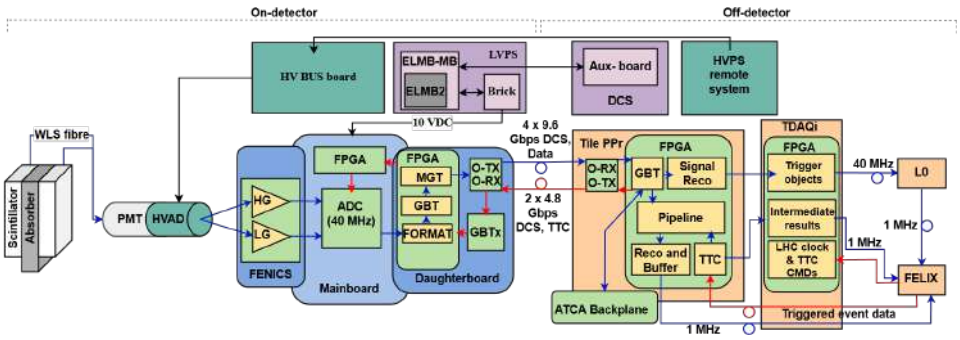


FIGURE 3.4: The phase II upgrade electronics [30].

3.1 Phase II upgrade architecture

3.1.1 Mechanics

In the upcoming Phase-II, TileCal is planning to improve accessibility, and robustness, and reduce the possible single point of failure by replacing the current drawer structures with mini-drawers (MD). These new mechanical structures will be 70 cm long and half the length of the current drawers. In the upgraded detector, a super-drawer will be composed of four separate mini-drawers. Each mini-drawer will consist of up to 12 PMTs, up to 12 Front-End-Cards (FENICs), 1 Main Board, 1 Daughter Board, and 1 HV passive distribution board. Each mini-drawer will have its individual power and signal pathways to the back-end electronics. Within the EB, there will be three mini-drawers and two micro-drawers, which solely serve to secure the PMTs in place and do not contain any digital circuitry.

3.1.2 Main board (MB)

An MB is located within each MiniDrawer (MD) of TileCal. A single MB is connected to twelve FENICS and one Daughter Board (DB). The mainboard is

690 mm by 100 mm in size [27]. Six PMT signals are sent in from each side, and the A-side and B-side regions of the mainboard are physically separated. The electronics on both sides are totally self-contained, with each side having its own +10V LVPS power supply brick. The mainboard electronics are divided into four portions, each of which is served by a separate FPGA. For better data alignment, the FPGA may also produce ADC test patterns. Six channels of 40 Msps 12-bit ADCs and three channels of 50 KHz 16-bit ADCs for the slow integrators are used to support the three PMTs in a section [31]. The phase of the signal sampling clocks can be adjusted to compensate for path length delays between MB and DB. All electronics on the MB are commercial off-the-shelf components. Low-gain and high-gain ADCs, as well as input bias voltage levels, are controlled by an Altera Cyclone EP4CE10F17 FPGA.

[1]

3.1.3 Daughter Board (DB)

The DB plays a crucial role in the Phase-II upgrade of the on-detector TileCal electronics, serving as both the read-out link and control board. It is designed with redundancy, divided into two independent halves (side A and side B). Redundant output links are incorporated on each side to ensure reliable communication. The DB has undergone multiple revisions, with recent versions powered by redundant 10VDC sources through connections routed via the MB. Point-of-load regulators or DC-DC converters provide the necessary voltages for efficient power distribution.

[1] Msps - Mega-samples per second

For the High-Luminosity LHC (HL-LHC) era, the upgrade plan entails the development of around 1000 radiation-tolerant DBs. These DBs facilitate the delivery of full-granularity digital data to an off-detector fully-digital trigger system using multi-Gbps optical fibers. Each DB establishes communication with off-detector systems through four 9.6 Gbps uplinks and two 4.8 Gbps downlinks. They enable high-speed read-out of digitized samples from Photomultiplier Tubes (PMTs) while managing configuration, control, and LHC-synchronous timing distribution to the front-end system. The DB design focuses on minimizing radiation-induced errors and enhancing data reliability through a fully double-redundant approach. It utilizes CERN radiation-hard GBTx ASICs and Xilinx FPGAs, implements Triple Mode Redundancy (TMR), applies Soft Error Mitigation (SEM) to correct configuration memory Single Event Upsets (SEUs), and incorporates Cyclic Redundancy Check (CRC) and Forward Error Correction (FEC) for data integrity in the uplinks and downlinks.

3.1.4 Auxiliary (AUX) board

All auxiliary signals and additional voltages for one branch of four LVBOXes are generated by the AUX Board. The power source is 230V AC mains. There are twelve isolated power supplies on the board. Four for ELMB motherboards (trimmed between 6.8 and 14.5V), four for ELMB chips (trimmed between 6.8 and 14.5V), and four for LVPS bricks' start-up signals (15 to 25V). It also has current loop sources for remote on/off control of the LVBOX HV/DIG side. Interlock circuitry is also a part of the AUX board. A clock generator and distributor are included on the AUX Board enabling the synchronous

functioning of all four supervised LVBOXes' DC/DC converters. The AUX board is controlled by its own ELMB module, which is programmed with a custom version of the ELMB firmware. All of the AUX boards are wired into their own CAN bus network nodes. Their control is integrated into the remote control system as a whole.

3.1.5 The Front-End board

A critical component of the Tile Calorimeter system is the TileCal Front-End board. It is responsible for the TileCal detector's initial stages of signal processing and data collecting. The Front-End board is intended to communicate with the scintillating tiles and photomultiplier tubes (PMTs), which detect and convert particle energy into electrical signals. This board handles a variety of tasks, including amplification, shaping, and digitization of PMT signals. It guarantees that the signals are correctly prepared for future processing and analysis. To ensure precise data collecting, the Front-End board also handles synchronization and timing tasks. The Front-End board includes circuitry for control and communication in addition to signal processing. It communicates with the readout system, allowing data and requests to be transmitted between the TileCal detector and the data acquisition system. The TileCal Front-End board has been intended to endure the extreme radiation environment and high particle flux encountered in high-energy physics experiments. It is important to obtain accurate energy measurements and to the overall performance of the TileCal system in the ATLAS detector at the Large Hadron Collider (LHC).

3.1.6 Photomultiplier blocks

Approximately 10% of the PMTs situated in the PMT blocks will be swapped out due to aging. The PMT blocks can be accurately situated in front of their corresponding WLS fiber bundles. Each PMT block has a cylindrical composition, incorporating a light mixer, a photomultiplier, a high-voltage divider, and a FENICS card. The mechanical structure is made up of steel, iron, and μ-metal to safeguard the PMTs and electronics against residual magnetic fields of up to 500 Gauss emanating from the ATLAS toroids. A light mixer is situated between each fiber bundle and the corresponding PMT photocathode to enhance the uniformity of light detection. Besides dispensing various high voltages to the PMT dynodes, the HV divider also provides connections between the PMTs and the FENICS cards through the PMT base sockets

3.1.7 High Voltage Power Supply

The PMTs obtain power from the High Voltage Power Supply (HVPS), which is composed of 256 electronically identical sub-modules. These sub-modules deliver a shared voltage via an off-detector HV source, which can generate a current of 20 mA and a voltage of -700 V, -900 V, or -1100 V. To ensure linearity under high luminosity, active dividers will replace the current passive dividers utilized to manage the high PMT current. The HV distribution system will be managed remotely from the HV regulation board, which is now known as the HV remote board. Located outside of the detector's radiation environment in the USA15 cavern, the regulation board prototypes have been evaluated and determined to satisfy the HV stability criteria.

Chapter 4

LVPS system

4.1 Introduction

The LVPS system consists of three devices: finger Low Voltage Power Supplies (fLVPS) situated at the Tile Calorimeter's FE electronics, auxiliary boards (AUX boards) located in USA15 racks, and bulk power supplies delivering 200V DC also located in USA15 racks. The LVPS system has two stages: the first converts 400V AC into 200V DC output in USA15, and the second stage on the detector converts 200V DC into 8 independent levels of lower voltages in the range (-15V; +15V) used to power the detector Front End (FE) electronics (the digital and analog components of the readout system and High Voltage (HV) distribution system.

Figure 4.1 shows the Phase-II architecture for the 3-in-1 option, with a demonstrator analog trigger. The Main Board and daughter board were discussed in more detail in Chapter 3.

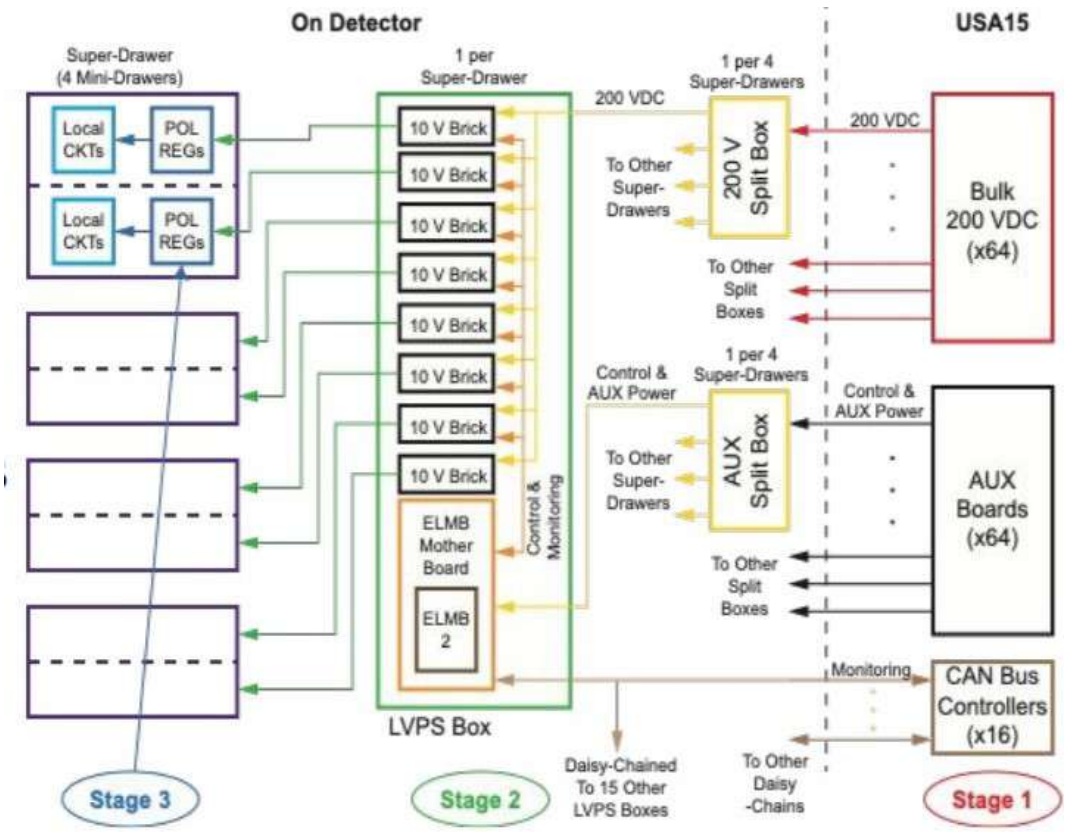


FIGURE 4.1: Schematic of the low voltage power distribution system. [32].

4.2 DC/DC Switching Power Supply Module - LVPS Brick

The LVPS bricks depicted in figure 4.4 are a component of the Tile Calorimeter's electronics in the ATLAS experiment of the LHC. Each TileCal wedge's Low Voltage Power Supply system comprises eight nearly identical power supply modules (bricks) linked in parallel, ensuring that all eight power supplies adhere to the same specifications and performance requirements. Due to the harsh operating environment (radiation hardness) and high-reliability demands, a custom-designed switching power supply was necessary. The LVPS

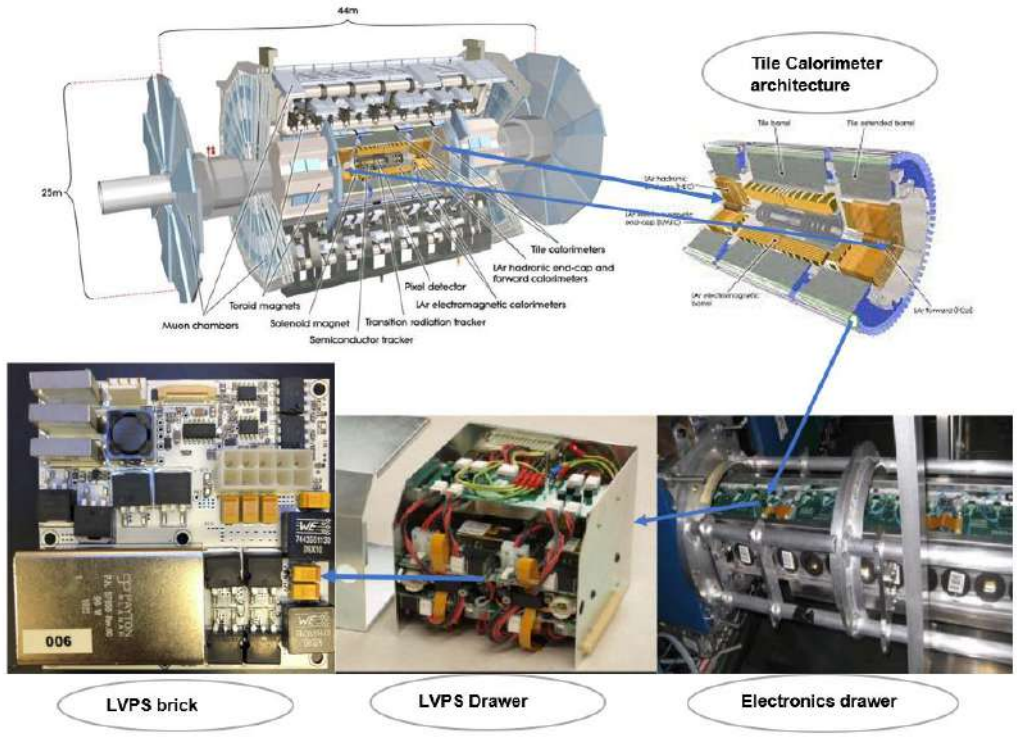


FIGURE 4.2: Systematic diagram showing the location of the LVPS brick in the ATLAS detector

must endure radiation hardening against single-event upsets and the total dose accumulated over multiple years in its environment. The system is composed entirely of Commercial off-the-shelf (COTS) components, is radiation tolerant up to 40 krad, and can function in a DC magnetic field exceeding 0.02 T [33]. The systematic diagram in figure 4.2 provides a clear depiction of the placement and integration of the LVPS brick within the ATLAS detector. It highlights the specific location of the LVPS brick within the detector's overall structure, illustrating how it interfaces with other components and subsystems to provide power to the on-detector electronics. Extensive irradiation tests of COTS components and the brick prototype are therefore required. LVPS also

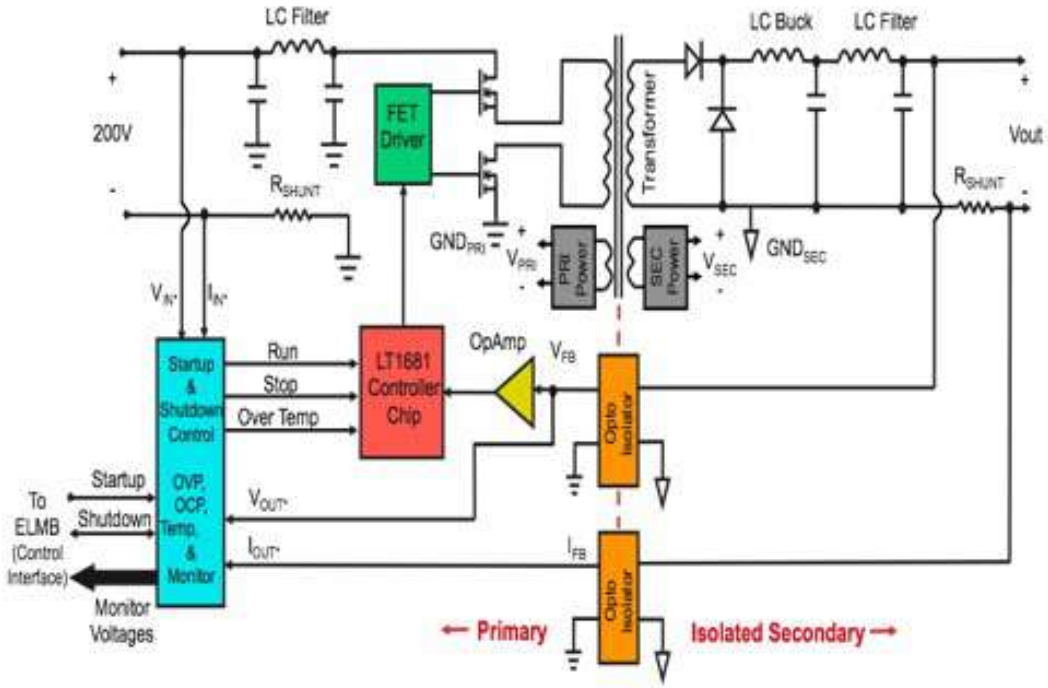
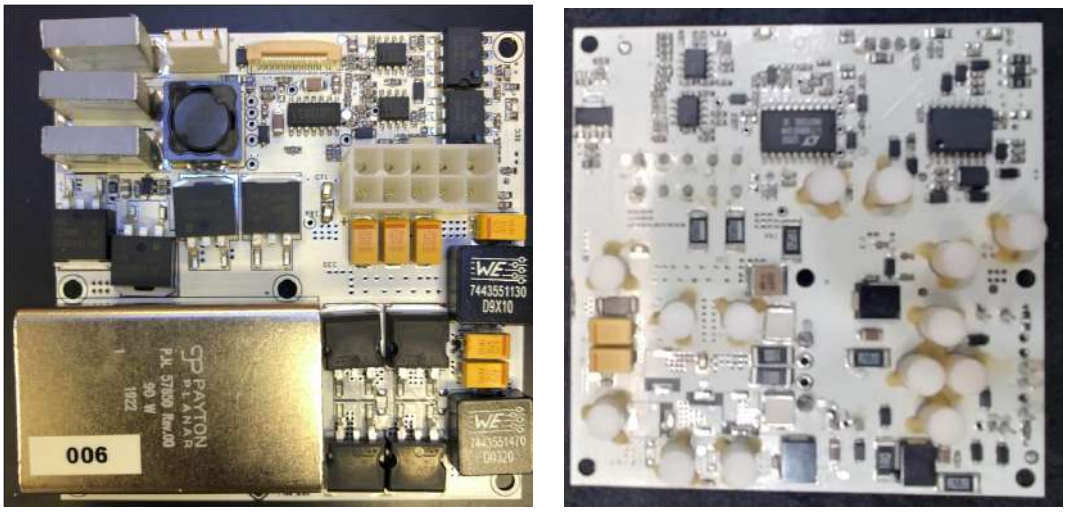


FIGURE 4.3: Systematic diagram of the LVPS brick [34].

includes specially designed magnetic components that enable reliable operation within the ATLAS magnetic field.

The systematic diagram in figure 4.3 of the LVPS brick provides a visual representation of the components and connections within the brick. The LVPS bricks, which provide power to all of the detector electronics, are designed to step down from 200 V to 10 V and have a nominal power rating of 100 W each [34]. They use a DC/DC converter based on an LT1681 chip dual transistor forward converter with a switching frequency of 300 kHz, and include various features such as limited size of LVBOX (170 x 170 x 170 mm), water cooling, remote independent On/Off for two functional parts of the drawer (HV side and Digitizer), remote monitoring of electrical parameters and temperatures, remote trimming of output voltages within +/-0.5V, local protection



(A) LVPS front-view. (B) LVPS back-view.

FIGURE 4.4: Wits Low Voltage power supply brick. The LVPS is custom-built using only COTS (Commercial Off-The-Shelf) components). (a) Shows the brick front view and (b) is the back view of the brick.

circuits (OVP, OCP, and OTP), safety interlock circuit, and increased reliability for power and signal distribution system due to limited-access during operation [33]. The Embedded Local Monitor Board motherboard sends an Enable signal and a start-up pulse to the brick. The start-up pulse supplies momentary power to the brick's control circuits, allowing it to turn on. Each brick will be tested using different methods to determine the efficiency of each LVPS and each brick must meet a number of requirements. The initial test station and the Burn-in test station are used for these tests. The Burn-in test station is discussed in detail in this thesis.

4.2.1 Low voltage power distribution

The Tile Calorimeter's LVPS system delivers power to all of the ATLAS Tile Calorimeter's front-end electronics as well as feedback and control via a monitoring system. Each super-drawer is powered by a single LVPS box, which can power up to four mini-drawers within the drawer. This gives the Tile a total of 256 LVPS boxes. The LVPS box is made up of eight bricks, which are independent power supply boards, a fuse board, and a monitoring/control board. There is also a water-cooled cold plate that runs laterally through the middle of the LVPS box. A 200V circuit supply located in the USA15 cavern powers each LVPS box. The updated brick design retains the same box size, water-cooled cold plate, and general footprint as the existing system. However, there are two notable differences in the new design. Firstly, instead of using eight different types of bricks with varying voltages and currents, the new design will utilize only one type of brick that converts the 200 V input voltage to a 10 V output voltage for all loads. Individual load voltages will be generated using point-of-load regulators located at the loads and derived from the brick output voltage. The second significant distinction is that redundancy will be built into the design, with the eight bricks being divided into four groups of two.

4.2.2 200VDC Bulk Power Supplies

The 200V Bulk Power Supply (200V PS) takes 400V AC and produces 200V DC, which is sent into the fLVPS devices through pin 80. In USA15, the 200V PS devices are housed in racks. Each 81 unit has three output channels, each of which feeds four fLVPS. The Extended and Long Barrel 83 of the Tile

Calorimeter have nominal output voltages of 82 200V and nominal usage of 4A and 5A, respectively, for the FE electronics (maximal output current 8.5A). In order to fully power 256 LVBOXes in the ATLAS PIT, we need 64 channels, so that is 22 HPS1 power supplies.

Chapter 5

Burn-in test station

5.1 Introduction

The LVPS brick undergoes a burn-in test, which is an electrical stress test that utilizes voltage and/or temperature to accelerate the discovery of hidden reliability flaws in an electronic device. The aim of this test is to identify and eliminate potential failures that may arise during the early stages of the brick's life cycle, also known as Infant Mortality Failure. The burn-in test station is utilized to perform endurance tests on the low-voltage power supply for extended periods. These tests ensure that the bricks can function effectively under normal conditions when installed in the Tile calorimeter at CERN, Geneva. The reliability bathtub, depicted in figure 5.1, is a standard graphical representation of the lifetime of a population of electronic components, consisting of three main stages: infant mortality, normal/"useful life," and end-of-life wear-out.

- **Infant mortality**

  This represents the initial phase of the curve, where the failure rate is decreasing. Burn-in testing can be utilized to effectively reduce the operational failure rate of the components by eliminating infant mortality failures. At this stage, the components are failing due to defects and errors such as material defects, assembly mistakes, and design errors.

- **Normal/"Useful life"**

  This is the second/middle phase of the curve where failures remain low and constant. During this period, the components are considered to be failing due to random issues, such as when the stress on the components exceeds their strength.

- **End of life wear-out**

  In the third period of the reliability bathtub curve, the failure rate begins to increase. This is attributed to the depletion of materials, which leads to wear and tear of the components.

5.2 Burn-in test station electronic hardware

5.2.1 Printed Circuit Boards (PCBs)

The burn-in test station is made up of various PCBs (Mainboard (×1), Brick interface (×8), Load interface (×2) and Dummy load (×2)), water chiller, a PC running LabView 2020, high voltage power supply and Chassis (contains all the electronic components of the burn-in test station, the cooling plates

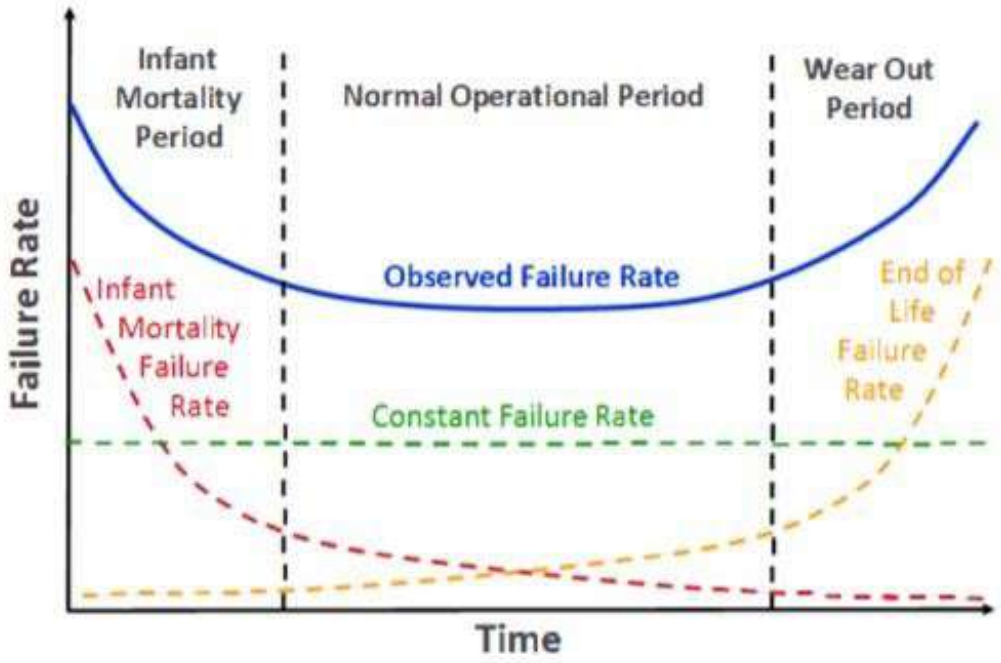


FIGURE 5.1: The reliability bathtub curve showing the three main periods, infant mortality, normal/"useful life" and end-of-life wear-out.

as well as the LVPS bricks). All PCBs of the Burn-in test station will be discussed in the following subsections including their main functions. [1]

5.2.2 Mainboard

The LabView software of the PC communicates directly with each microprocessor via UART. This communication is established by utilizing an FTDI IC and a serial link over a USB virtual COM port. The main board acts only as a multiplexer for each individual read-out board, these boards will be discussed later. To connect with a specific interface board (0-9), the PC asserts the RTS (Request to Send) flag on the UART level and transmits the address. After

[1]The mainboard discussed in this section is not the readout mainboard discussed in section 3.1.2.

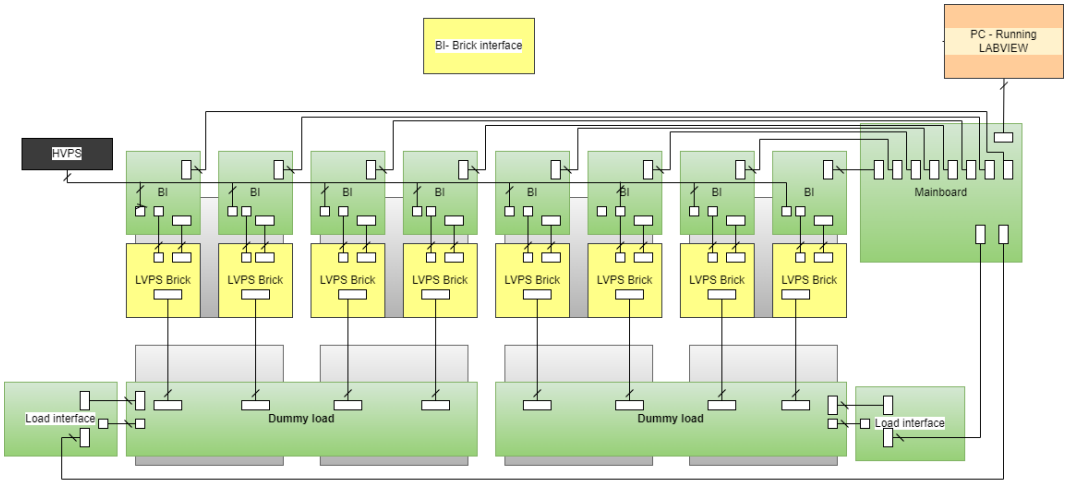


FIGURE 5.2: Block Diagram of Burn-in Test Station showing Interconnections among PCBs (Mainboard, Brick Interface, Load Interface, and Dummy Load) and High Voltage Power Supply

unasserting the RTS flag, LabView on the PC achieves multiplexing. Once the address is initialized, all bytes transmitted from the PC are directly delivered to the corresponding read-out board without any intervention or interference from the main board.

5.2.3 Brick Interface

The brick interface board has four connectors on each of its two ends. One end is utilized for linking the high-voltage power supply (200V supply) and the main board (15V supply), while the other end is utilized for connecting to the low-voltage power supply. The primary function of the brick interface board is to convert analog signals to digital signals and transmit them to the PC. To achieve this, each board has an analog-to-digital converter from linear technology. Sixteen brick interface boards were manufactured for two burn-in test stations, with each low-voltage power supply having its own brick interface



FIGURE 5.3: The Burn-in test station Brick interface board.

board. The MODULE board supplies the brick with a Vstartup voltage of +15V and +5V for powering the brick thermistors. The brick interface board is a fully independent and isolated brick control board from other brick interface boards. It also contains voltage dividers for the thermistors located on the brick to prevent temperature drift of the thermistor voltage divider circuit.

5.2.4 Load Interface

The load interface board shares the same PCB design as the brick interface board. Its purpose is to establish communication between the mainboard and the electronic load, as depicted in the block diagram in figure 5.2. A populated load interface PCB can also be seen in the figure. The load interface board reads the brick differential voltages and currents from the electronic load's four channels. These analog signals are converted to digital format using a 10-bit 16-channel ADC. The data is then processed by a PIC16F883 microcontroller



FIGURE 5.4: Two Burn-in test station dummy load interface.

before being transmitted to the mainboard, which acts as a multiplexer. The mainboard is connected to the PC via a high-speed USB 2.0 interface. To enable the PCBs to perform their respective tasks, the PIC microcontroller must be programmed to issue commands for each board.

5.2.5 Dummy load

A burn-in test station consists of two dummy loads which uses 4 VCCs that uses high precision op-amps and N-channel MOSFET. Each dummy load board is connected to four bricks and it provides a controllable load current of up to 10 A. It functions as a variable electronic load for the LVPS bricks, converts

power received into heat through the MOSFETS and the heat dissipated via cooling plates.

5.3 Software

5.3.1 Embedded firmware

All of the interface boards' firmware was written in embedded-C. Both the brick interface board and the load interface board used a state machine. This project demonstrates how to use a PIC microcontroller to carry out straightforward communication using an RS232 interface. A typical serial communication interface is RS232, which allows data to be obtained and transmitted via at least three wires. Through the RS232 interface, a link between a microcontroller and a PC, via the PC's COM port. The RS232 is used for a variety of tasks, including sending commands from a PC to a microcontroller, relaying debugging information from a microcontroller to a terminal, and downloading new firmware to the microcontroller. A terminal program will be integrated into the PC to receive and transfer data. The terminal window displays data sent by the microcontroller, and any keys pressed therein will send the corresponding key code to the microcontroller.

5.4 PIC16F883 microcontroller

The PIC16F883 microcontroller processes the data from the brick interface, mainboard, interface board, load interface board, and dummy load. In this section, the PIC16F883 will be discussed in more detail. The legacy software of the burn-in test station used a PIC16F877. The change to PIC16F833 meant that the legacy PIC microcontroller C code must be modified. Figure 5.5 shows the PIC16F883 microcontroller (left) and the pin diagram of the

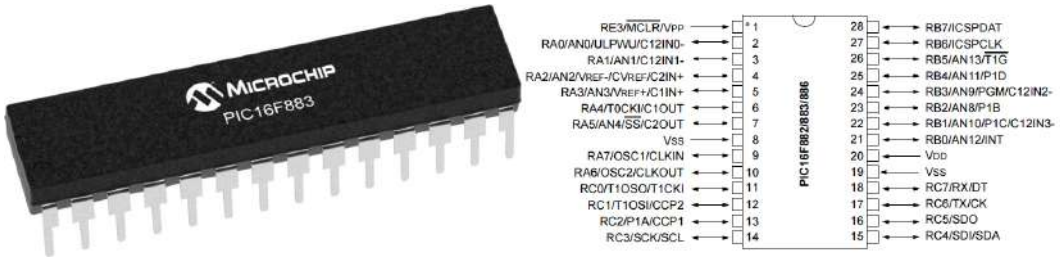


FIGURE 5.5: The PIC16F883 microcontroller (left) and the pin diagram of the microcontroller (right).

microcontroller (right).

The PIC16F883 microcontroller has the following characteristics:

- Consists of 28 pins.
- There are 24 I/O lines.
- Voltage range of the supply: 2V to 5V.
- RISC architecture (35 instructions).
- Program memory: 4kB FLASH
- An external oscillator (up to 20 MHz) or an internal 8 MHz.
- Data memory: 256 bytes SRAM, 256 bytes EEPROM
- 10-bit A/D converter, 3 counters/ timers, 2 analog comparators, a serial port and a parallel port controlled by hardware, Watchdog Timer etc.

Instead of using the LTC2449 ADC which is used on the final product of the burn-in test station in the simulation the LTC2440 ADC was used. The reason behind this replacement is that the Proteus software does not have a simulator version for LTC2449 ADC. This is fine as they have similar features.

The main difference between these two versions of ADCs is that the LTC2440 does not have a multiplexer and for that reason, additional channels cannot be addressed such as with the LTC2449. The LTC2440 is a 24-Bit High-Speed Differential Delta Sigma ADC with Selectable Speed/Resolution, featuring a 5 ppm INL, 5 uV offset, and no latency. It makes use of a unique delta-sigma design that allows for latency-free adjustable speed and resolution.

The PIC16F883 is manufactured by Microchip. The Harvard architecture, which employs distinct memories for program and data, is used by the Microchip microcontrollers (independent buses). The program memory is of the OTP or FLASH type. The data memory is of the RAM type, and both direct and indirect addressing is possible. Most types of microcontrollers from Microchip have also a memory of the EEPROM type. The PIC16F833 microcontroller belongs to the group of 8-bit microcontrollers. All memory cells as well as internal registers of the microcontroller have therefore a width of 8 bits. These memory cells are collectively called registers.

5.4.1 Load-interface board circuitry simulation in Proteus 8

Proteus software is a valuable tool for designing, drawing and simulating electronic circuits, allowing for simulation of circuits before physical implementation. This reduces the risk of damaging electronic components. The firmware is compiled using a CCS compiler in MPLABX IDE, generating a hexadecimal (hex) format source file that contains machine code to program the PIC microcontroller. The load interface board is simulated in Proteus ISIS using this hex file, to confirm the firmware works efficiently before programming the

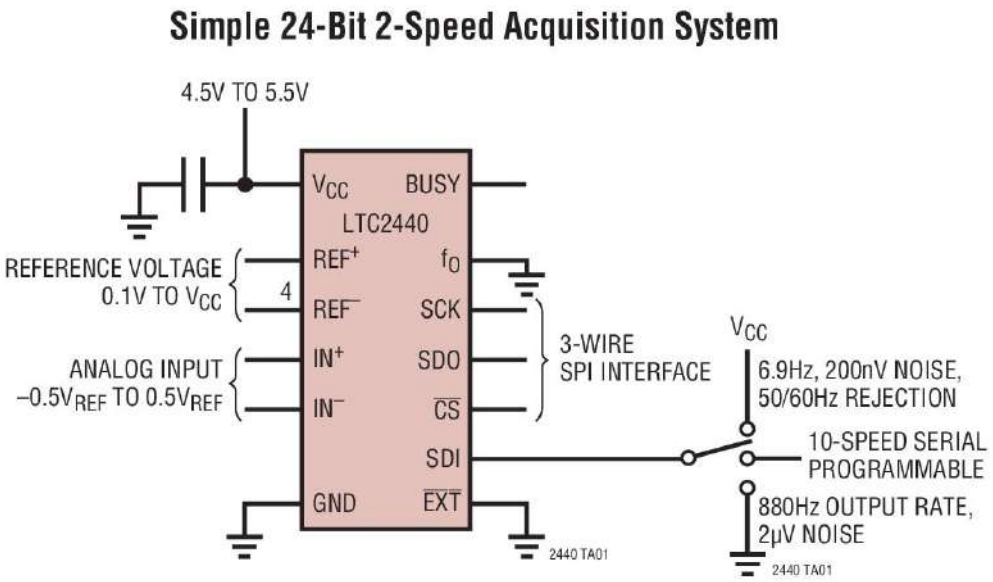


FIGURE 5.6: LTC2440 ADC.

hardware. The properties of components must be set to emulate hardware properties, such as the frequency and crystal oscillator set to 16MHz for the PIC16F883. In the simulation, ASCII characters are used in the switch statement of the firmware to turn the LED on and off. "h" is used for switching on the LED, and "l" for switching it off. The ASCII character "q" is used on the virtual terminal of Proteus software to read back the module address, which should be unique for each module. The load interface circuit is also designed to read analog signals through the ADC channels, converting the analog signal into binary information sent to the microcontroller for processing and display on the virtual terminal as digital information. [2]

[2]The hex file is generated in the CCS compiler after the C code is built successfully.

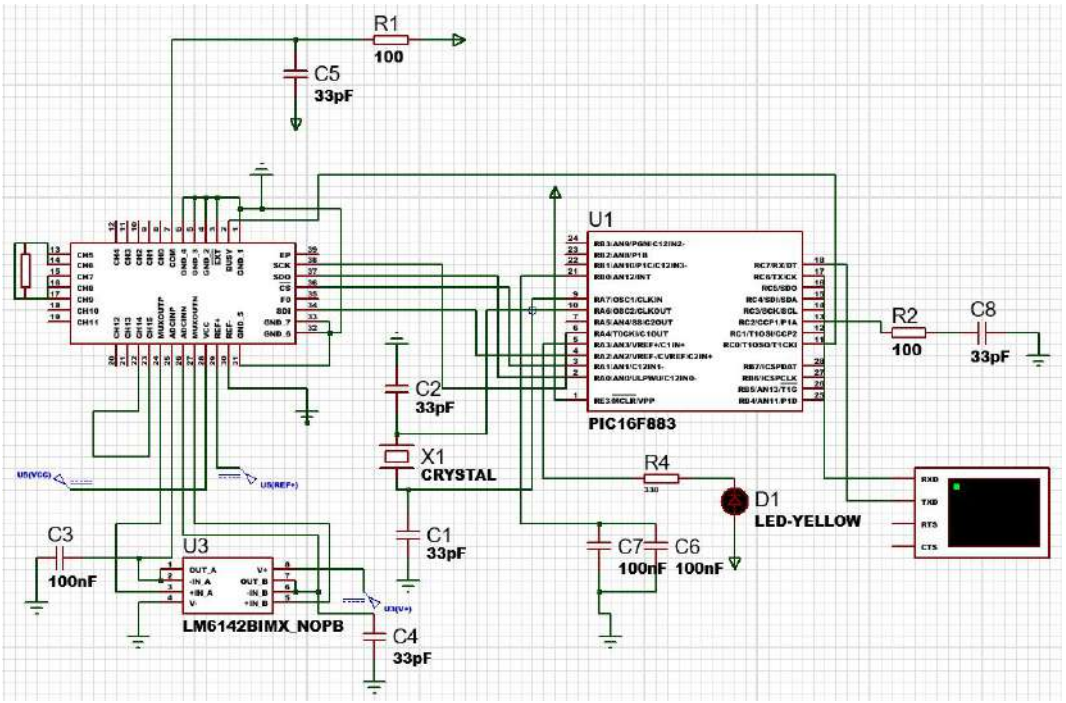


FIGURE 5.7: In Proteus, a load interface circuit was created to simulate the PIC C microcontroller firmware.

LabView control program

LabVIEW program plays an important role in the functionality of the LVPS brick BURN-IN test station. LabVIEW program communicates with all eleven microprocessors in the burn-in test station through a single UART layer link passed over a USB. This program was modified from the legacy program of CERN. Labview custom drivers were installed in order to accomplish communication with the high-voltage power supply. We use this software to set the loads, enter the brick information, create a text file where the collected data will be stored for each brick, and start/stop the test. Figure 5.8 is a diagram of the LabView program's front graphical interface. The brick's efficiency and temperature are displayed on the front panel in real-time. For each brick, the input, output and load (currents and voltages) values are also shown. The user

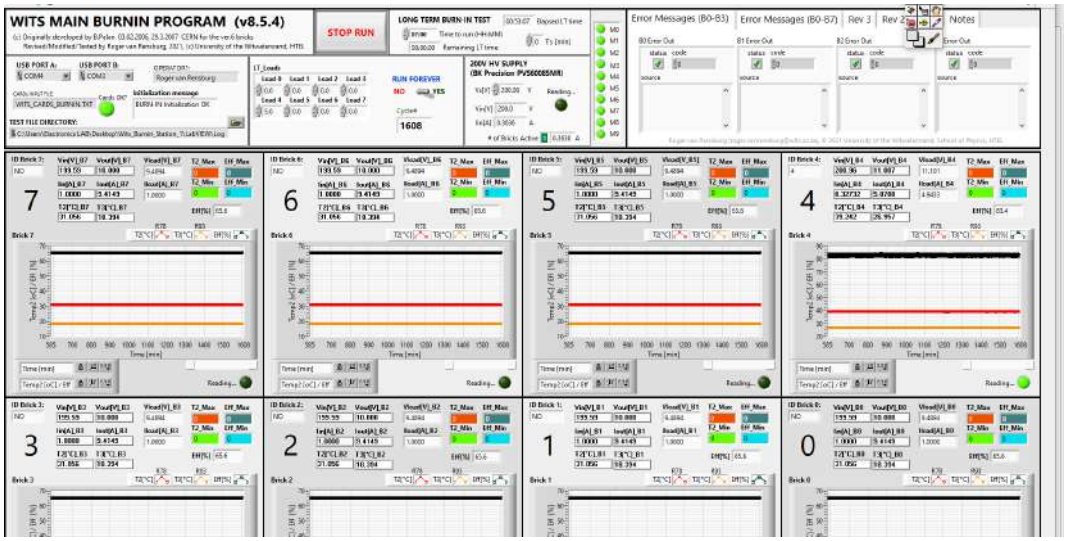


FIGURE 5.8: Labview graphic user interface (Front panel).

can stop the test at any time via the front panel. In LabVIEW, the efficiency plots and temperature plots are recorded in real-time.

5.5 Method(s)

5.5.1 Programming the PIC16883 microcontroller

The following tools and software are required for PIC microcontroller programming:

- The assembler (MPLABX IDE) and a compiler (CCS). This is the software package that also includes the debugger (PICkit 4).
- A PC is used to run the development program.
- A PIC16F883 microcontroller.

  A programmer is a physical device that connects to a computer by serial, parallel, or USB line. The PIC is placed into the programmer and

uploaded by downloading the development system's executable code. A cable or connector (rs232 serial communication cables) for connecting the programmer to the computer.

- Breadboard.
- Breadboard wires.
- Hex file containing the commands for the PCBs.

A legacy PIC C code was used for programming the PIC microcontrollers with some modifications made. For prototyping breadboarding was used. A breadboard is a reusable, solderless device that can be used to produce a prototype circuit for testing purposes. Breadboards have strips that serve as power rails on one or both sides. One strip carries the circuit's positive voltage, while the other is connected to the power supply's ground. For constructing circuit connections on the breadboard, wire jumper kits contain connectors of various lengths and colours.

5.5.2 Burn-in test station Procedure for the LVPS brick testing.

The test bed contains eight Low Voltage Power Supply bricks. Each run of the test lasts for about six hours preferably. The burn-in test station can test up to 8 bricks per run but it can be used to test less than 8 bricks for each run. The purpose of the burn-in process is to verify that the LVPS bricks meet the technical specifications of CERN, detect any systematic issues, identify any failed components, and induce early failure in electronic components by

subjecting them to accelerated aging. This aging is achieved by exposing the brick to elevated load and temperature conditions. The burn-in test is crucial for quality assurance to confirm the dependability of the construction and design of the low-voltage power supply brick. The test setup consists of eight LVPS bricks, and each test run is typically six hours in duration. Six hours is used for burn-in testing because it provides a reasonable duration to subject the LVPS bricks/components to accelerated aging conditions and identify any potential defects or failures that might occur during normal operation.

Bricks per run	8
Temperature	60-80 °C
Brick load	10 A
Duration	6 hour(ideally)

TABLE 5.1: Burn-in test station operating conditions.

5.6 Results

5.6.1 Temperature monitoring using Themography

Electrical thermography plays an important role in electronics as faulty electrical equipment has been known to start fires, which can seriously harm the environment/ electronic devices and put people's lives in danger. Using heat distribution images obtained through thermography, electrical and mechanical equipment can be inspected. This inspection technique is based on the observation that most system components become hotter when they are malfunctioning. When it comes to mechanical equipment, worn bearings or loose connections may be responsible for a rise in temperature in an electrical circuit. Faults can be found and their severity assessed by looking at the heat

patterns in operating system components.

Across the electromagnetic spectrum, a heated object emits energy at various wavelengths and intensities. The energy radiated at infrared wavelengths is typically utilized in industrial applications to gauge an object's temperature. The electromagnetic spectrum contains a variety of radiated energy forms including Infrared, Ultra Violet, X-ray, and radio. The wavelengths interval of 0.4 to 0.75 m is where the human eye reacts to visible light. Most infrared temperature measurements are conducted between 0.2 and 20 m in size. The science of collecting and analyzing thermal data from non-contact thermal imaging sensors is known as infrared (IR) thermography. IR thermography uses the electromagnetic spectrum's infrared region to detect radiation that has been emitted. This corresponds to wavelengths outside of the range of visible light. Figure 5.9 shows the electromagnetic spectrum with the visible and infrared regions zoomed out.

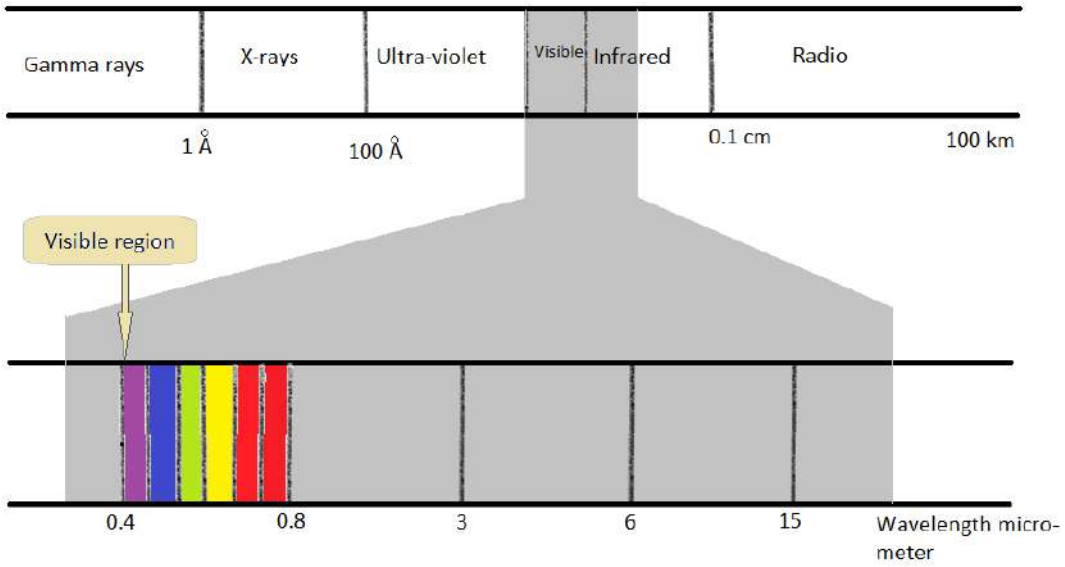


FIGURE 5.9: The visible and infrared regions of the Electromagnetic spectrum zoomed out.

Figure 5.10 is the thermogram showing one Low Voltage Power Supply "brick" operating in the Burn-in test station. Purple and black on the thermogram represent the cold areas, yellows and white are warm areas and red is the hot areas. As can be observed in the image most of the brick area is red, this is expected as the brick's operation components temperature increases. Cooling plates are used for the thermal management of LVPS brick. The water chiller circulates cold water into the plates.

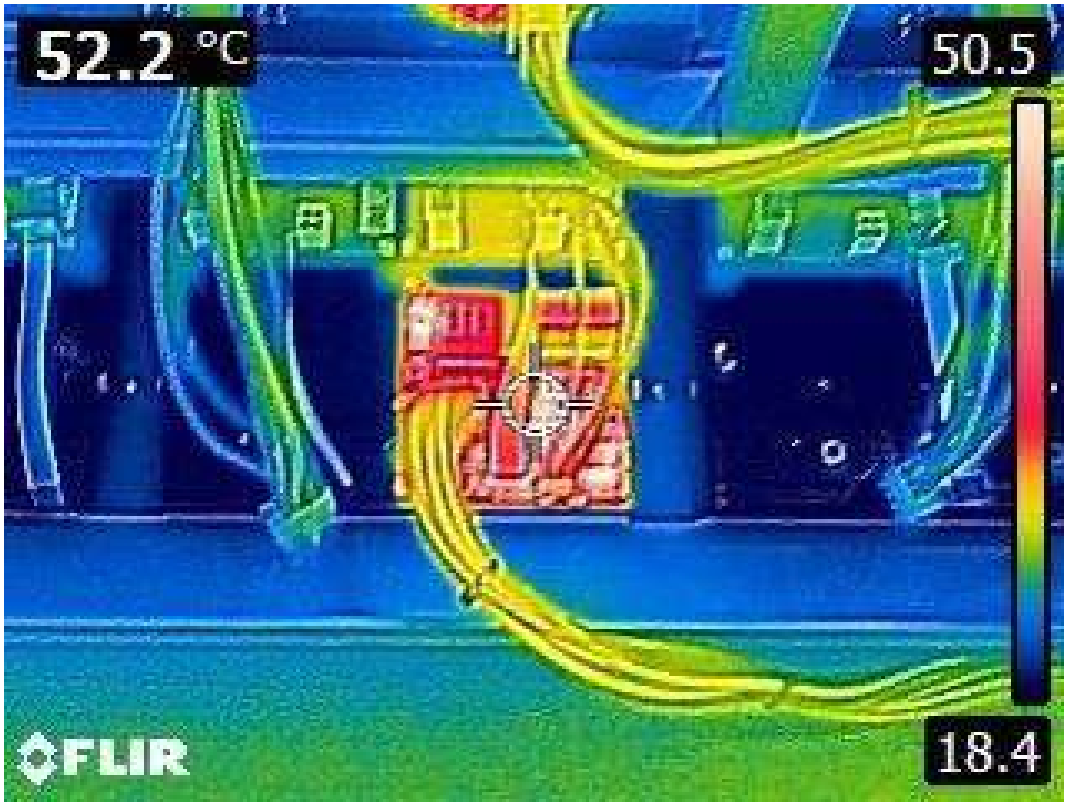


FIGURE 5.10: Thermogram showing one Low Voltage Power Supply "brick" operating in Burn-in test station.

5.6.2 Monitoring the LVPS brick and high voltage power supply voltages and currents.

It is essential to measure power supply efficiency accurately in electronics. A power supply's reliability is directly impacted by its efficiency. The LVPS brick uses a water-cooling system for thermal management. Burn-in test station use a water cooling circuit to elevate the temperature of the brick to source away power from a load of all 8 bricks. Low power losses and less heat generation from the power supply will also assist other critical system components. The inefficiency of the LVPS brick can be estimated by the amount of heat it produces. When the brick is operational and gets hot, all that heat is evidence



FIGURE 5.11: Dummy load operating in burn-in station

of lost power and reduced efficiency. Some power loss can be due to the power needed to keep the brick operational.

$$Efficiency = \frac{P_{out}}{P_{in}} \tag{5.1}$$

Where P_{out} is the useful output power and P_{in} is the total power input. Efficiency does not have units as it is a ratio of one quantity of power to another. Efficiency is normally specified as a percentage:

$$Efficiency = \frac{P_{out}}{P_{in}} \times 100\%. \tag{5.2}$$

Electrical power (Watts) in equation 5.2 is given by:

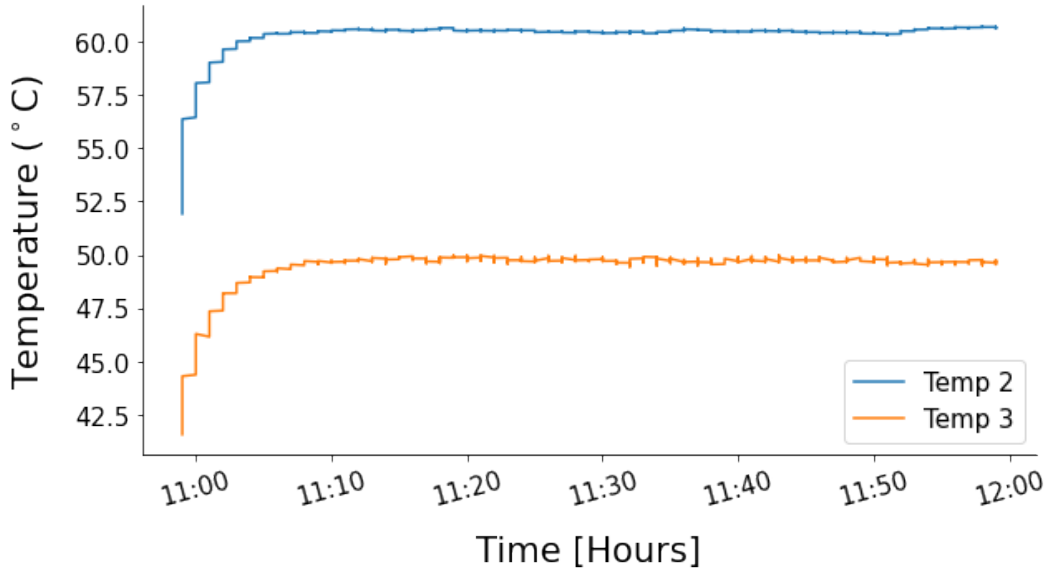


FIGURE 5.12: Temperature 2 stability plot for the LVPS brick.

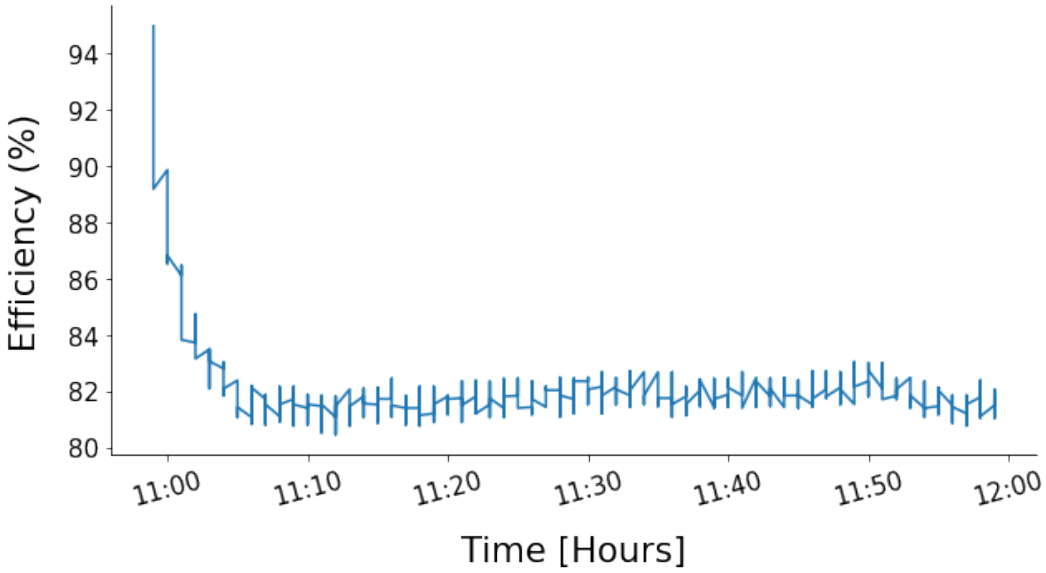


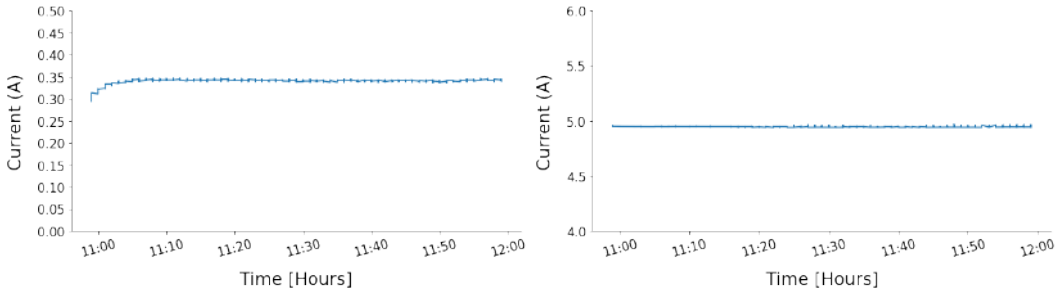
FIGURE 5.13: Temperature 2 stability plot for the LVPS brick.

$$P = V \times I \tag{5.3}$$

- V - Voltage

- I - Current

The efficiency calculations for the LVPS brick are automatically calculated using the LabVIEW program. The efficiency plot against time is shown in figure 5.13. Comparing the efficiency plot with the temperature plots it is evident that efficiency is dependent on temperature and time. The data was collected every 2 seconds for 3648 seconds with the brick operational on the burn-in test station. The brick efficiency was stable at around 81% with T2 and T3 fluctuating around 50°C and 60°C respectively. These results are good for this particular LVPS brick because this means less power is being wasted as heat and this has a huge contribution to the reliability of electronic components. Therefore it is clear that efficiency plays a big role in the reliability and lifetime of the LVPS brick. Efficiency was measured at a high ambient temperature and load. Other parameters (load, input and output currents and voltages) were also monitored during the burn-in test. The LVPS brick also undergoes various tests using a test station to verify these parameters. For more details regarding these tests refer to reference [35]. Looking at the results from the burn-in test, the measured parameters fall within the limits listed in table 5.2. The LVPS brick is a DC-DC buck converter, this means it will reduce voltage and increase current. Looking at figure 5.14a and figure 5.14b we can see that this statement holds true. Figure 5.15a show the set voltage (200 V) from the BK Precision PVS60085MR high voltage power supply against time. In figure 5.15b, the voltage received by the LVPS brick is slightly more than the set voltage (1%). This can also be said about the set current and load current of the brick as expected, this is shown figure 5.16a and figure 5.16b. Figure 5.17a and figure 5.17b plots represent the output and load voltages of the brick and



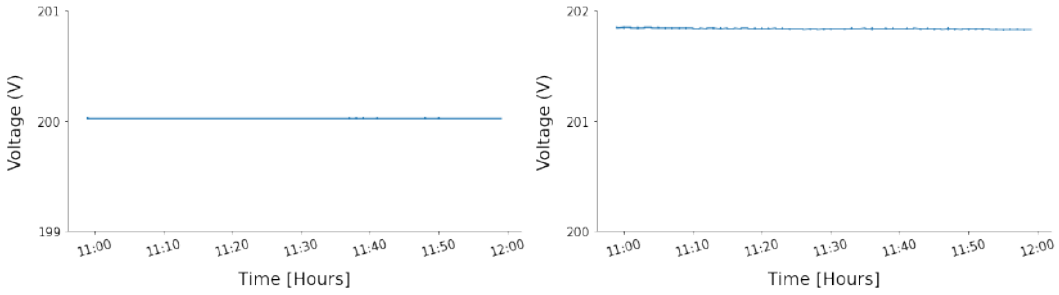
(A) Brick input current against time . (B) Brick output current against time .

FIGURE 5.14: Comparison of the brick input and output current against time.

Parameter	Minimum	Maximum
Frequency Standard Deviation (Hz)	0	1000
Frequency Max (Hz)	290000	350000
Frequency Min (Hz)	250000	310000
Minimum Stable Load (A)	0	2.3
Minimum Output Voltage (V)	9.8	10.9
Over Voltage Protection Trip Point (V)	11.5	12
Over Current Protection Trip Point (A)	10.25	10.75
Duty Cycle Standard Deviation (%)	0	0.1
Clock Duty Cycle Average (%)	0	45
Clock Duty Cycle Standard Deviation (%)	0	0.15
Maximum Start-up Delay (s)	0.2	0.08

TABLE 5.2: A list of LVPS brick test parameters limit responses for output measurements [35].

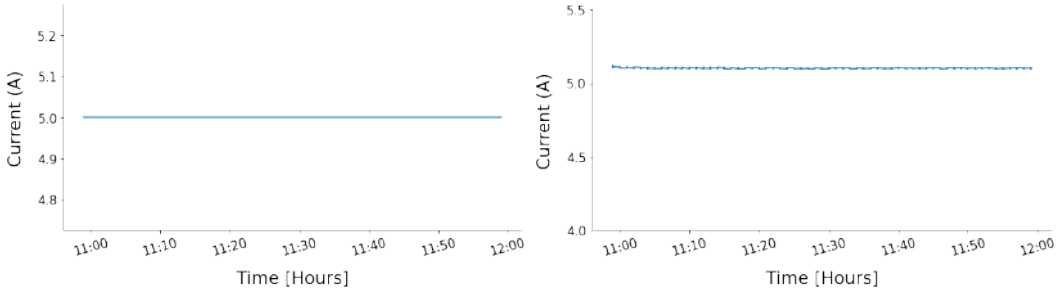
the voltage is stable at 11.0 V, this value is within the limits listed on the LVPS table 5.2. This means the brick did not trip during the duration of the test. The Over Voltage Protection trip points are 11.5 V–12 V and the Over Current Protection trip points for the LVPS are 10.25–10.75 A.



(A) Set voltage on the programmable HV power supply against time .

(B) Input voltage received by the LVPS brick over the duration of the test.

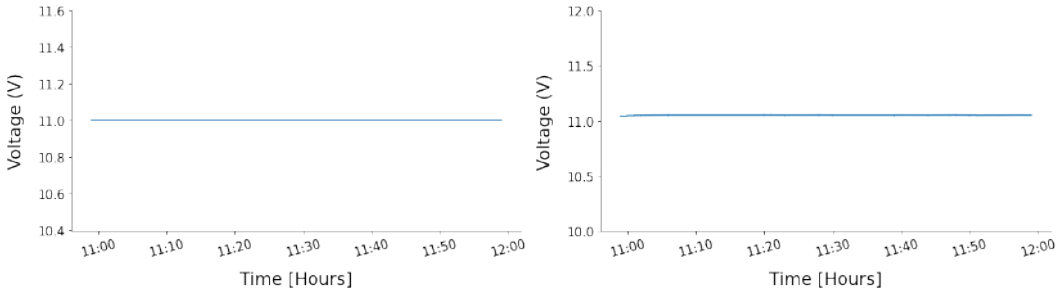
FIGURE 5.15: Comparison of the LVPS brick input voltage with the set voltage by the high voltage power supply over time.



(A) Brick set current (Iset) against time .

(B) Brick load current (Iload) against time .

FIGURE 5.16: Comparing the brick set current and load current of the LVPS brick against time.



(A) Brick output voltage against time .

(B) Brick output load voltage against time.

FIGURE 5.17: Comparison of the LVPS brick output and output load against time.

Chapter 6

Conclusion

6.1 LVPS brick production

In conclusion, the University of the Witwatersrand plays a significant role in producing LVPS bricks, which are required for powering the on-detector electronics of the TileCal in the ATLAS detector. The institution is diligently putting together plans for pre-production and preparing for the manufacturing process. The results of thorough testing and analysis of the 8.4.2 version of the LVPS brick are covered in this thesis. Some bricks have already been sent to CERN for further testing before being installed into the ATLAS detector. The LVPS brick version 8.4.6 will be produced during the pre-production phase and will include a few changes meant to improve efficiency. Notably, in order to increase efficiency, a considerable alteration will be made to the power MOSFET, a vital part of the brick. This modification represents the ongoing effort to improve the bricks' functionality and performance to meet the ATLAS detector's stringent requirements. The contribution to the creation of LVPS bricks, the University of the Witwatersrand has demonstrated dedication to cutting-edge research and technological innovation while also making

a substantial contribution to the field of particle physics. The institution is prepared to play a crucial role in extending the capabilities of the ATLAS detector, ultimately advancing our understanding of the fundamental building blocks of the universe, through collaboration with CERN and dedication to enhancing the bricks' efficiency.

6.2 Burn-in test station hardware and software

In preparation for the pre-production and the main production, two burn-in test station are being developed in order to verify that the specification requirements of the bricks meet the minimum requirements to operate in the detector's environment thus they must have high efficiency. One burn-in test station is completed and a second burn-in test station will be an exact replica of the current burn-in test station. During the development of the burn-in test station, a simulation of the circuit was used in proteus 8 software to verify that the PIC microcontroller C code works efficiently. The PIC C code is written in MPLABX IDE using a CCS compiler for microcontrollers and a hex file is generated and uploaded to the PIC16F883 microcontroller of each PCB to allow the boards to perform their respective functions. To check if the firmware works efficiently, ASCII characters were sent using Real-Time serial communication program to turn ON/OFF the LED in the circuit. The firmware used in the simulation is a legacy firmware, so some functionalities were removed and the code was modified to work with new components used on the PCBs. The modifications were also made to the Labview legacy program including some changes on the front-end panel and installing the drivers to

control the HV power supply. The efficiency of the brick is automatically calculated by Labview and a txt file is generated by the program with different brick parameters.

6.3 Results

The results of the stress test of the LVPS brick version 8.4.2 in this study have produced positive results. The bricks were subjected to a stress test that featured high temperatures, notably T2 and T3, which were set at 50°C and 60°C, respectively. This test was designed to evaluate the bricks' performance and hardness under challenging thermal conditions.

The thermogram provides a visual representation of the temperature distribution across the surface of the brick, allowing for a comprehensive assessment of its thermal behavior. Upon analysis of the thermogram results presented in Figures 5.10 and 5.11, it is evident that the findings are in agreement with the measured T2 results obtained from the brick thermistors. The observed correlation between thermogram results and measured T2 values supports the stress test's validity and demonstrates that the LVPS brick version 8.4.2 functions as expected under the stipulated elevated temperature conditions. This result is critical in assuring the brick's capacity to withstand and operate effectively in the ATLAS detector's extreme environment.

These findings provide insight into the thermal properties and stability of the

LVPS bricks, supporting their potential for powering the TileCal in the ATLAS detector's on-detector electronics. These bricks show promising potential for reliable and efficient operation within the detector system by showing satisfactory performance during stress testing.

While the results of LVPS brick version 8.4.2 are encouraging, more testing and analysis are required to evaluate and confirm the robustness of these findings. Future research could include more extensive stress testing under various operating situations to evaluate the bricks' performance and reliability.

Overall, the findings of the stress testing of LVPS brick version 8.4.2, combined with the correlation between thermogram results and observed T2 values, provide a solid foundation for the LVPS bricks' continued development and optimization. These findings contribute to the ATLAS detector's continuing upgrade.

Bibliography

[1] Lyndon Evans and Philip Bryant. "LHC Machine". In: *Journal of Instrumentation* 3.08 (2008), S08001–S08001. DOI: 10.1088/1748-0221/3/08/s08001. URL: https://doi.org/10.1088/1748-0221/3/08/s08001.

[2] Giorgio Apollinari et al. *High-luminosity large hadron collider (HL-LHC): Preliminary design report*. Tech. rep. Fermi National Accelerator Lab.(FNAL), Batavia, IL (United States), 2015.

[3] Georges Aad et al. "Improved luminosity determination in pp collisions at $\sqrt{s} = 7$ TeV using the ATLAS detector at the LHC". In: *The European Physical Journal C* 73.8 (2013), pp. 1–39.

[4] P La Rocca and F Riggi. "The upgrade programme of the major experiments at the Large Hadron Collider". In: *Journal of Physics: Conference Series*. Vol. 515. 1. IOP Publishing. 2014, p. 012012.

[5] Sijiye Humphry Tlou. "Implementation of the Stopless removal software for the Level-1 Tile-Muon Trigger system of the LHC ATLAS TileCal". PhD thesis. Faculty of Science, University of the Witwatersrand, 2019.

[6] Samah Abdel Khalek Abdel khalek. "Measurement of the total proton-proton cross section with ATLAS at LHC". Theses. Université Paris Sud - Paris XI, Nov. 2013. URL: https://tel.archives-ouvertes.fr/tel-00962261.

[7] S. Chatrchyan et al. “The CMS experiment at the CERN LHC”. In: *Journal of Instrumentation* 3 (Aug. 2008), S08004.

[8] S. Chatrchyan et al. “The CMS Experiment at the CERN LHC”. In: *JINST* 3 (2008), S08004. DOI: 10.1088/1748-0221/3/08/S08004.

[9] Antonio Alves et al. “A Roadmap for HEP Software and Computing RD for the 2020s”. In: *Computing and Software for Big Science* 3 (Mar. 2019). DOI: 10.1007/s41781-018-0018-8.

[10] Christian Lippmann. “Particle identification”. In: *Nucl. Instrum. Methods Phys. Res., A* 666 (2011). 61 pages, 30 figures, 148–172. 61 p. DOI: 10.1016/j.nima.2011.03.009. arXiv: 1101.3276. URL: http://cds.cern.ch/record/1323010.

[11] Eduardo Ros. “ATLAS inner detector”. In: *Nuclear Physics B - Proceedings Supplements* 120 (2003). Proceedings of the 8th International Conference on B-Physics at Hadron Machines, pp. 235–238. ISSN: 0920-5632. DOI: https://doi.org/10.1016/S0920-5632(03)01908-X. URL: https://www.sciencedirect.com/science/article/pii/S092056320301908X.

[12] Daniel Fournier and Tejinder Virdee. “The ATLAS and CMS detectors at the LHC”. In: *Comptes Rendus Physique* 16.4 (2015). Highlights of the LHC run 1 / Résultats marquants de la première période d’exploitation du GCH, pp. 356–367. ISSN: 1631-0705. DOI: https://doi.org/10.1016/j.crhy.2015.03.018. URL: https://www.sciencedirect.com/science/article/pii/S1631070515000699.

[13] Georges Aad et al. “Alignment of the ATLAS Inner Detector in Run 2”. In: *The European Physical Journal C* 80.12 (2020), pp. 1–41.

[14] Alexandre Solodkov. “Electrons, photons, and muons in ATLAS”. In: *EPJ direct* 4.1 (2002), pp. 1–2.

[15] ATLAS collaboration et al. “The ATLAS Inner Detector commissioning and calibration”. In: *arXiv preprint arXiv:1004.5293* (2010).

[16] Stephen Haywood. “The ATLAS inner detector”. In: *Nuclear Instruments and Methods in Physics Research Section A: Accelerators, Spectrometers, Detectors and Associated Equipment* 408.1 (1998), pp. 242–250.

[17] Sandro Palestini. “The muon spectrometer of the ATLAS experiment”. In: *Nuclear Physics B-Proceedings Supplements* 125 (2003), pp. 337–345.

[18] Herman Kate. “ATLAS Superconducting Toroids and Solenoid”. In: *Applied Superconductivity, IEEE Transactions on* 15 (July 2005), pp. 1267 –1270. DOI: 10.1109/TASC.2005.849560.

[19] Akira Yamamoto et al. “The ATLAS central solenoid”. In: *Nuclear Instruments and Methods in Physics Research Section A: Accelerators, Spectrometers, Detectors and Associated Equipment* 584 (Jan. 2008), pp. 53–74. DOI: 10.1016/j.nima.2007.09.047.

[20] Herman Kate. “The ATLAS Superconducting Magnet System: Status of Construction Installation”. In: *Applied Superconductivity, IEEE Transactions on* 16 (July 2006), pp. 499 –503. DOI: 10.1109/TASC.2006.871348.

[21] Djamel Eddine Boumediene. *Timing for the ATLAS Phase-II Upgrade*. Tech. rep. ATL-COM-LARG-2020-031, 2020.

[22] CMS Collaboration et al. "Measurement of the inelastic proton-proton cross section at $\sqrt{s} = 13$ TeV". In: *Journal of High Energy Physics* 07 (Jan. 2018).

[23] A. Sivolella et al. "Tile-in-ONE: A web platform which integrates Tile Calorimeter data quality and calibration assessment". In: *Journal of Physics: Conference Series* 664 (Dec. 2015), p. 052034. DOI: 10.1088/1742-6596/664/5/052034.

[24] Jared David Little. *The ATLAS Tile Calorimeter Phase-II Upgrade Demonstrator Data Acquisition and Software*. Tech. rep. ATL-COM-TILECAL-2018-046, 2018.

[25] Jasmin Abdallah et al. *The optical instrumentation of the ATLAS Tile Calorimeter*. Jan. 2013. DOI: 10.1088/1748-0221/8/01/P01005.

[26] Kai Siegbahn and E Karlsson. *Nuclear Instruments and Methods in Physics Research. Section A: accelerators, spectrometers, detectors and associated equipment. Volume A249, No. 1*. Tech. rep. Missouri Univ., Columbia (USA), 1986.

[27] *Technical Design Report for the Phase-II Upgrade of the ATLAS Tile Calorimeter*. Tech. rep. Geneva: CERN, 2017. URL: https://cds.cern.ch/record/2285583.

[28] Ryan Peter Mckenzie. "The ATLAS Tile Calorimeter performance and its upgrade towards the High-Luminosity LHC." In: (2021). URL: https://cds.cern.ch/record/2764513.

[29] A Henriques. "The ATLAS tile calorimeter". In: *2015 4th International Conference on Advancements in Nuclear Instrumentation Measurement Methods and their Applications (ANIMMA)*. IEEE. 2015, pp. 1–7.

[30] Ryan Peter Mckenzie. *Upgrade of ATLAS Hadronic Tile Calorimeter for the High Luminosity LHC*. Tech. rep. Geneva: CERN, 2021. DOI: 10.22323/1.397.0246. URL: http://cds.cern.ch/record/2781520.

[31] Eduardo Valdes Santurio et al. "Upgrade of Tile Calorimeter of the ATLAS detector for the High Luminosity LHC." In: *Journal of Physics: Conference Series*. Vol. 928. 1. IOP Publishing. 2017, p. 012024.

[32] E. Nkadimeng et al. "A monitoring and control test bench for assessing the upgraded low voltage power supplies for the ATLAS Tile Calorimeter Phase-II Upgrade front-end electronics". In: *Journal of Instrumentation* 17.07 (2022), P07025. DOI: 10.1088/1748-0221/17/07/P07025. URL: https://dx.doi.org/10.1088/1748-0221/17/07/P07025.

[33] I Hruska et al. "Radiation-Tolerant Custom Made Low Voltage Power Supply System for ATLAS/TileCal Detector". In: (2007). DOI: 10.5170/CERN-2007-007.369. URL: https://cds.cern.ch/record/1091490.

[34] Michael Hibbard et al. "ATLAS TileCal low voltage power supply upgrade hardware and testing". In: *Nuclear Instruments and Methods in Physics Research Section A: Accelerators, Spectrometers, Detectors and Associated Equipment* 936 (2019), pp. 112–114.

[35] E Nkadimeng et al. "A monitoring and control test bench for assessing the upgraded low voltage power supplies for the ATLAS Tile Calorimeter

Phase-II Upgrade front-end electronics". In: *arXiv preprint arXiv:2205.03374* (2022).